

Simulated last deglaciation of the Barents Sea Ice Sheet primarily driven by oceanic conditions

Michele Petrini^{a,i,*}, Florence Colleoni^a, Nina Kirchner^{b,c}, Anna L.C. Hughes^{d,e}, Angelo Camerlenghi^a, Michele Rebesco^a, Renata G. Lucchi^a, Emanuele Forte^f, Renato R. Colucci^g, Riko Noormets^h, Jan Mangerud^d

^a*OGS (Istituto Nazionale di Oceanografia e Geofisica Sperimentale), Borgo Grotta Gigante 42/c, 34010 Sgonico (TS), Italy*

^b*Bolin Centre for Climate Research, Stockholm University, SE-106 91 Stockholm, Sweden*

^c*Department of Physical Geography, Stockholm University, SE-106 91 Stockholm, Sweden*

^d*Department of Earth science, University of Bergen and Bjerknes Centre for Climate Research, N-5007 Bergen, Norway*

^e*Department of Geography, University of Manchester, Oxford Rd M13 9PL Manchester, UK*

^f*Dipartimento di Matematica e Geoscienze, Università di Trieste, via Weiss 1, 34128 Trieste (TS), Italy*

^g*ISMAR (Istituto di Scienze Marine), Trieste, Italy*

^h*The University Centre in Svalbard (UNIS), P.O. Box 156 Northern-9171 Longyearbyen, Norway*

ⁱ*Now at Department of Geoscience and Remote Sensing, Delft University of Technology (TUDelft), Delft, Netherlands*

Abstract

The Barents Sea Ice Sheet was part of an interconnected complex of ice sheets, collectively referred to as the Eurasian Ice Sheet, which covered north-westernmost Europe, Russia and the Barents Sea during the Last Glacial Maximum (around 21 ky BP). Due to common geological features, the Bar-

[☆]List of Abbreviations: LGM = Last Glacial Maximum, SIS = Scandinavian Ice Sheet, BIIS = British-Irish Ice Sheet, BSIS = Barents Sea Ice Sheet, WAIS = West Antarctic Ice Sheet, MISI = Marine Ice Sheet Instability, MICI = Marine ice-cliff instability, mLHS = maxi-min Latin Hypercube Sampling, AOGCM = Atmosphere-Ocean General Circulation Model, SIA = Shallow Ice Approximation, SSA = Shallow Shelf Approximation

*Corresponding author. Tel.: +39 3398367372

Email address: mpetrini139@yahoo.it (Michele Petrini)

ents Sea component of this ice complex is seen as a paleo-analogue for the present-day West Antarctic Ice Sheet. Investigating key processes driving the last deglaciation of the Barents Sea Ice Sheet represents an important tool to interpret recent observations in Antarctica over the multi-millennial temporal scale of glaciological changes. We present results from a perturbed physics ensemble of ice sheet model simulations of the last deglaciation of the Barents Sea Ice Sheet, forced with transient atmospheric and oceanic conditions derived from AOGCM simulations. The ensemble of transient simulations is evaluated against the data-based DATED-1 reconstruction to construct minimum, maximum and average deglaciation scenarios. Despite a large model/data mismatch at the western and eastern ice sheet margins, the simulated and DATED-1 deglaciation scenarios agree well on the timing of the deglaciation of the central and northern Barents Sea. We find that the simulated deglaciation of the Barents Sea Ice Sheet is primarily driven by the oceanic forcing, with prescribed eustatic sea level rise amplifying the ice sheet sensitivity to sub-shelf melting over relatively short intervals. Our results highlight that the sub-shelf melting has a very strong control on the simulated grounding-line flux, showing that a slow, gradual ocean warming trend is capable of triggering sustained grounded ice discharge over multi-millennial timescales, even without taking into account marine ice sheet or ice cliff instabilities.

Keywords: Quaternary, Glaciology, Barents Sea, Ice sheet modelling, Ocean melting

1. Introduction

During the Last Glacial Maximum (LGM, around 21 ky BP) an interconnected complex of ice sheets covered Northern Eurasia, forming a continuous ice cover extending from the Atlantic continental shelf south-west of Great Britain to northeast of Franz Josef Land, over the Kara Sea. This complex, collectively referred to as the Eurasian ice sheets, comprised three large ice sheets: the Scandinavian Ice Sheet (SIS), the British-Irish Ice Sheet (BIIS) and the Barents Sea Ice Sheet (BSIS) (Hughes et al., 2016). The former two ice sheets were predominantly terrestrial, whereas the BSIS was almost entirely marine-based (Fig. 1). As first observed by Mercer in the early 1970s (Mercer, 1970), the BSIS shares common geological features with the present-day West Antarctic Ice Sheet (WAIS). In fact, the two ice sheets have similar size, are located in high polar regions and have their base resting on a relatively soft sediments bed.

Several recent studies show that over the last decades marine-terminating glaciers and ice shelves of the WAIS are rapidly retreating (Cook et al., 2016; Rignot et al., 2013) and thinning (Paolo et al., 2015), primarily due to the intrusion of relatively warm Circumpolar Deep Water in the cavities underneath the ice-shelves and close to the grounding zone (Rignot et al., 2013; Pritchard et al., 2012; Schmidtko et al., 2014; Khazendar et al., 2016), although there is also evidence in favor of surface warming (Rebesco et al., 2014a). However, to what extent ice-shelf thinning or collapse might trigger sustained grounded ice discharge into the ocean remains highly uncertain, precluding well-constrained future projections of the WAIS contribution to future global-mean sea level rise (Edwards et al., 2019; Colleoni et al., 2018).

26 Both ice sheet modelling studies and observations suggest that ice-shelf thin-
27 ning or collapse in West Antarctica can potentially trigger two positive feed-
28 back effects, marine ice-sheet instability (MISI (Schoof, 2012; Rignot et al.,
29 2014; Favier et al., 2014; Joughin et al., 2014)) and marine ice-cliff instability
30 (MICI (DeConto and Pollard, 2016; Pollard et al., 2015)), leading in turn to
31 widespread, accelerated and sustained mass loss. However, the use of existing
32 parametrisations to represent these feedbacks in ice sheet model simulations
33 is still debated, as it might lead to an overestimated ice sheet response to
34 ocean warming (Gudmundsson et al., 2012; Petrini et al., 2018; Edwards
35 et al., 2019). Direct measurements of the dynamic response of the WAIS to
36 ocean warming are difficult to acquire because of the large spatio-temporal
37 scale of glaciological changes (Colleoni et al., 2018). A valid alternative to
38 fulfil this knowledge gap is to look at evidence of past ice sheet retreats
39 both in the Northern and Southern Hemisphere. In this study, we focus on
40 the last deglaciation of the BSIS. Paleo data show that after reaching its
41 maximum extent during the LGM, the BSIS experienced a relatively rapid,
42 stepwise retreat, leaving the Barents and Kara seas continental shelf ice-free
43 around 14 ky BP (Hughes et al., 2016). Available marine geophysical data
44 provide insights on the ice sheet dynamics and retreat patterns throughout
45 the deglaciation. Therefore, the last deglaciation of the BSIS represents an
46 excellent testing ground to validate the ability of ice sheet models to repro-
47 duce fast transitions, in order to better constrain the evolution of the WAIS
48 in response to global warming.

49 In this study, we present results from a perturbed physics ensemble of
50 100 transient simulations of the BSIS during the last deglaciation. The sim-

51 ulations are performed with the GRenoble Ice Shelf and Land Ice model
52 (GRISLI (Ritz et al., 2001)), a zero-order hybrid model (Kirchner et al.,
53 2011) which is able to simulate ice sheet/stream/shelf systems. In order to
54 evaluate the response of the marine-based BSIS to ice shelf thinning result-
55 ing from ice-ocean interactions, we explicitly compute sub-shelf melting by
56 means of a two-equations formulation, based on a quadratic, local depen-
57 dency of melting rates on the ocean thermal forcing (Holland et al., 2008).
58 This formulation, similar to that used in the ice sheet model simulations
59 contributing to the ISMIP6 projections for the Antarctic Ice Sheet (Barthel
60 et al., 2019; Seroussi et al., 2019), has shown a good agreement with coupled
61 ocean-ice sheet simulations under idealised future ocean warming scenarios
62 (Favier et al., 2019).

63 In order to prevent possible biases in increased sub-shelf melting rates
64 due to the ice physics response, GRISLI does not include any of the existing
65 parametrisations for MISI and MICI feedbacks (Gudmundsson et al., 2012;
66 Petrini et al., 2018; Edwards et al., 2019). To reduce uncertainties due to
67 poorly constrained ice sheet model parameters, we perform a maxi-min Latin
68 Hypercube Sampling (mLHS) of five parameters, related to the surface eleva-
69 tion feedback, ice dynamics and sensitivity to ocean warming. An ensemble
70 of 100 transient simulations is performed, each run with a different combina-
71 tion of the selected model parameters. This perturbed physics ensemble of
72 simulations is first tested against the data-based deglacial chronologies from
73 the DATED-1 archive (Hughes et al., 2016). We select a group of simulations
74 in the ensemble satisfying minimal requirements of ice sheet extent model-
75 data agreement, and we use this group of simulations to construct minimum,

76 maximum and average deglaciation scenarios. These three scenarios are then
77 analyzed and compared with the DATED-1 deglacial chronologies.

78 **2. Glacial history of the Barents and Kara seas**

79 The Barents and Kara seas' continental shelf is characterised by a rela-
80 tively uneven bathymetry, alternating shallow banks (100-200 meters deep),
81 deep transverse troughs (300-500 meters deep) and several archipelagos (Sval-
82 bard, Franz Josef Land, Novaya Zemlya and Severnaya Zemlya, Fig. 1).
83 Geological records suggest that this region was repeatedly glaciated during
84 the late Cenozoic (Vorren et al., 1988), with several major glacial advances,
85 from which two glacial maxima (140 ky BP and 21 ky BP) occurring in the
86 last 160 kyrs (Svendsen et al., 2004). The LGM occurred during the Late
87 Weichselian (Svendsen et al., 2004; Landvik et al., 1998) between 25 and 23
88 ky BP, when ice masses over Svalbard, Novaya Zemlya and Franz Josef Land
89 coalesced into an integrated BSIS (Hughes et al., 2016).

90 Sediment cores from trough-mouth fans and offshore ice rafted debris
91 suggest that the western and northern margins of the BSIS extended up or
92 close to the continental shelf edge during the LGM (Landvik et al., 1998;
93 Andersen et al., 1996; Kleiber et al., 2000). Subsequent studies analyzing
94 data from the south-western, central and northern Barents Sea confirmed
95 this reconstruction (Fig. 1). In contrast, the extent of the eastern margin of
96 the ice sheet during the LGM has been debated since the late 1990s (Svend-
97 sen et al., 2004). The data-based reconstruction DATED-1 (Hughes et al.,
98 2016) suggests that the ice sheet extended over Novaya Zemlya in the eastern
99 Kara Sea, but never reached the mainland Russia and Siberia (Fig. 1), with

100 the exception of a short-lived advance of an ice lobe over the north-western
101 Taymyr Peninsula slightly prior than the LGM (Hughes et al., 2016). This
102 is in contradiction with previously published reconstructions based on glacial
103 isostatic adjustment modeling (Peltier, 2004; Peltier et al., 2015), claiming
104 that the ice sheet extent over north-western Taymyr in the north-east was
105 sustained during the LGM. In the south, there is no doubt that the BSIS
106 and the SIS were connected at the LGM, although the timing of coalescence
107 of these two ice sheets is not well constrained due to a lack of chronological
108 data (Hughes et al., 2016).

109 Marine geophysical data from the Barents Sea continental shelf and slope
110 show that during the LGM the BSIS was drained by several ice streams
111 flowing in cross-shelf throughs at the western and northern ice sheet mar-
112 gins (Landvik et al., 1998; Stokes and Clark, 2001; Ottesen et al., 2005;
113 Dowdeswell et al., 2010; Fransner et al., 2018, 2017; Rebesco et al., 2014b).
114 These paleo-ice streams are similar in size and velocity pattern to the ice
115 streams draining the present-day WAIS. In the south-western Barents Sea,
116 Bjørnøyrenna hosted the Bjørnøyrenna ice stream (Fig. 1), the largest ice
117 stream draining the ice sheet during the LGM (Andreassen and Winsbor-
118 row, 2009; Bjarnadóttir et al., 2014). Data suggest that the Bjørnøyrenna
119 ice stream had several tributaries extending into the central Barents Sea
120 (Sentralbankrenna in the east and Storbankrenna in the north, Fig. 1) and
121 throughout deglaciation the ice stream experienced changes in flow regime
122 and spatial switch of their flow (Bjarnadóttir et al., 2014; Piasecka et al.,
123 2016; Esteves et al., 2017; Newton et al., 2017). North of Bjørnøyrenna,
124 the Storfjorden ice stream extended up to the south-western Barents Sea

125 continental shelf edge on at least three occasions during the last 200 kyrs
126 (Llopart et al., 2015), including the LGM (Fig. 1) (Pedrosa et al., 2011;
127 Lucchi et al., 2013). Both the glacial drainage area and size of Storfjor-
128 den ice stream are relatively small compared to the Bjørnøyrenna ice stream
129 (Svendsen et al., 2004), and geophysical evidence suggest a strong climatic
130 control on its deglaciation (Lucchi et al., 2013; Nielsen and Rasmussen, 2018;
131 Shackleton et al., 2019). During the LGM, the northern margin of the Bar-
132 ents Sea was drained by several ice streams, with variable size and drainage
133 area, flowing in cross-shelf troughs/channels (Svendsen et al., 2004; Land-
134 vik et al., 1998; Dowdeswell and Siegert, 1999). In Kvitøya Trough (Fig.
135 1), streamlined landforms indicate the presence of warm-based, fast-flowing
136 ice, although modest elongation ratios suggest that ice-flow velocities were
137 relatively low compared to other drainage systems (Hogan et al., 2010a).
138 Signatures of fast ice flow are more prominent in Franz Victoria Trough,
139 indicating the presence of a major ice stream (Kleiber et al., 2000; Ottesen
140 et al., 2005; Polyak et al., 1997; Hogan et al., 2010b) (Fig. 1). Further east,
141 limited data from St. Anna Trough suggest that an ice stream occupied the
142 entire trough to the continental shelf edge during the LGM (Polyak et al.,
143 1997) (Fig. 1). However, the lack of bathymetric data from the north-eastern
144 Barents Sea and Kara Sea limits the current understanding of the ice sheet
145 dynamics in St. Anna Trough, as well as further east in Voronin Trough
146 (Hughes et al., 2016; Patton et al., 2015).

147 **3. Methods**

148 *3.1. Ice sheet model description*

149 The ice sheet model used in this study is the 3D zero-order (Kirchner
150 et al., 2011) thermo-mechanical model GRISLI (GRenoble Ice Shelf and Land
151 Ice model, (Ritz et al., 2001)). GRISLI is a hybrid shallow ice/shallow shelf
152 approximation model, able to simulate inland ice, ice streams, and floating
153 ice shelves. The stress regime is determined using the Shallow Ice Approx-
154 imation (SIA) (Hütter, 1983; Morland, 1984) for inland ice, whereas in ice
155 shelves and ice streams the ice deforms according to the the Shallow-Shelf
156 Approximation (SSA) and the “dragging ice shelf” extension of the SSA, re-
157 spectively (Kirchner et al., 2011; MacAyeal, 1989). During runtime, GRISLI
158 identifies ice shelf grid points according to a simple flotation criterion based
159 on Archimedes’ principle. Ice streams grid points are characterized by thick
160 sediment layers saturated by meltwater and areas with low effective basal
161 pressure (Ritz et al., 2001). The surface mass balance (SMB) over the ice
162 sheet is computed from the annual mean temperature and precipitation us-
163 ing the Positive-Degree-Days (PDD) semi-empirical method (Reeh, 1991).
164 GRISLI has been validated over Antarctica (Ritz et al., 2001) and applied
165 over multi-millennial timescales to simulate ice inception over Eurasia during
166 the Early Weichselian (Peyaud et al., 2007). The model version used in this
167 study is described in (Ritz et al., 2001) and includes the improvements pre-
168 sented in (Peyaud et al., 2007). Below, we summarise further modifications
169 we applied to the ice sheet model, whereas for a detailed, comprehensive
170 description of the ice sheet model used in this study we refer to (Petrini,
171 2017). Finally, it is highlighted for clarity that the GRISLI version and the

172 perturbed physics ensemble of simulations described in this study are the
 173 same as in (Petrini et al., 2018). However, (Petrini et al., 2018) analyze only
 174 one ensemble member showing the best fit against the ICE-5G reconstruction
 175 (Peltier, 2004). In this study, we analyze a different group of simulations,
 176 showing the largest agreement with the data-based deglacial chronologies
 177 from the DATED-1 archive (Hughes et al., 2016) (see Subsection 3.6).

178 • The annual snow accumulation (ACC) is computed from the annual
 179 mean total precipitation (P_a) following a precipitation conversion scheme
 180 from (Marsiat, 1994). In this formulation, a linear transition between solid
 181 and liquid precipitation depending on the annual mean air temperature (T_a)
 182 is assumed, yielding

$$\text{ACC} = I_f \cdot P_a, \quad (1)$$

183 where I_f is the solid/liquid precipitation fraction, defined as

$$I_f = \begin{cases} 1, & \text{if } T_a \leq -10^\circ\text{C}, \\ (7^\circ\text{C} - T_a) / 17^\circ\text{C}, & \text{if } -10^\circ\text{C} < T_a \leq 7^\circ\text{C}, \\ 0, & \text{if } T_a > 7^\circ\text{C}. \end{cases} \quad (2)$$

184 • The PDD method is highly sensitive to the daily temperature stan-
 185 dard deviation (σ), a parameter accounting for the temperature daily cycle
 186 (Reeh, 1991; Braithwaite, 1984). However, this parameter is not very well
 187 constrained and previous modeling studies focusing on the Greenland ice
 188 sheet assigned to σ a single value ranging between 2.5-5.5°C (Greve, 2005;
 189 Greve et al., 2011; Goelzer et al., 2011; Sundal et al., 2011). In this study,
 190 we consider the standard deviation of air temperature as a 3D variable by
 191 using an empirical parametrisation based on data from automatic weather

192 stations in Greenland (Fausto et al., 2011). The annual mean (σ_a) and July
 193 (σ_j) standard deviations of air temperature increase with the altitude (h)
 194 and also have a minor dependence on latitude (ϕ),

$$\sigma_a = 0.324 + 1.104 \cdot h + 0.0573 \cdot \phi, \quad (3)$$

195

$$\sigma_j = 2.220 + 1.259 \cdot h - 0.0178 \cdot \phi. \quad (4)$$

196 Given σ_a and σ_j , the standard deviation of air temperature σ is assumed to
 197 vary sinusoidally over time,

$$\sigma(t) = \sigma_a + (\sigma_j - \sigma_a) \cos \frac{2\pi t}{A}, \quad (5)$$

198 where A is one year. Once that σ is computed, the number of PDD is ob-
 199 tained using the standard formulation (Reeh, 1991).

200

201 • In the original PDD formulation (Reeh, 1991), the melt factors for snow
 202 (C_s) and ice (C_i) are assumed as constant in space and time. Here, we follow
 203 (Fausto et al., 2009; Tarasov and Richard Peltier, 2002) by introducing melt
 204 factors depending on the July mean air temperature T_j ,

$$C_i = \begin{cases} 17.22 \text{ mm/PDD}, & \text{if } T_j \leq -1^\circ\text{C}, \\ 0.0067 \cdot (10 - T_j)^3 + 8.3 \text{ mm/PDD}, & \text{if } -1^\circ\text{C} < T_j \leq 10^\circ\text{C}, \\ 8.3 \text{ mm/PDD}, & \text{if } T_j > 10^\circ\text{C}, \end{cases} \quad (6)$$

$$C_s = \begin{cases} 2.65 \text{ mm/PDD}, & \text{if } T_j \leq -1^\circ\text{C}, \\ 0.15 \cdot T_j + 2.8 \text{ mm/PDD}, & \text{if } -1^\circ\text{C} < T_j \leq 10^\circ\text{C}, \\ 4.3 \text{ mm/PDD}, & \text{if } T_j > 10^\circ\text{C}. \end{cases}$$

205 By using this formulation, we take into account the decrease/increase of
 206 the ice and snow melt factors with temperature due to the changing mix of
 207 radiative and turbulent surface energy fluxes (Tarasov and Richard Peltier,
 208 2002).

209 • Following (Pollard and DeConto, 2012), we use a parametrisation of the
 210 sub-shelf melting as a function of the far-field (*i.e.*, outside of ice-shelf cav-
 211 ities) ocean temperature and salinity. This empirical formulation (Holland
 212 et al., 2008) assumes a quadratic, local dependence of the sub-shelf melting
 213 rates on the heat exchanges at the ice-ocean boundary. The positive feed-
 214 back between the sub-shelf melting and the circulation in ice-shelf cavities is
 215 taken into account via the quadratic relationship (Holland et al., 2008). This
 216 formulation has been used in stand-alone ice sheet simulations and has shown
 217 a good agreement with coupled ocean-ice sheet simulations under idealised
 218 future ocean warming scenarios (Favier et al., 2019). The ice temperature at
 219 the ice-shelf draft (z_b , in meters) follows from the state equation of seawater
 220 freezing point (T_f),

$$T_f(z_b) = 0.0939 - 0.057 \cdot S_o(z_b) - 7.64 \cdot 10^{-4} \cdot z_b, \quad (7)$$

221 where S_o is the ambient ocean salinity. Given the ambient ocean temperature
 222 (T_o), the quadratic, local ocean thermal forcing H_f is obtained,

$$H_f = (T_o(z_b) - T_f(z_b)) \cdot |T_o(z_b) - T_f(z_b)|, \quad (8)$$

223 and used to compute the sub-shelf melting rate as follows,

$$b_m = \frac{\rho_0 c_o \gamma_t F_m}{\rho_i L_i} \cdot H_f, \quad (9)$$

224 where ρ_0 is the ocean water density, $c_o = 3974 \text{ J kg}^{-1} \text{ }^\circ\text{C}^{-1}$ is the specific
225 heat capacity of the ocean mixed layer, $\gamma_t = 1 \times 10^4 \text{ m s}^{-1}$ is the ocean
226 thermal exchange velocity, $\rho_i = 917 \text{ kg m}^{-3}$ is the ice density and $L_i =$
227 $3.35 \times 10^5 \text{ J kg}^{-1}$ is the ice latent heat capacity. Our choice of the values
228 assigned to the dimensionless model parameter F_m does not follow (Pollard
229 and DeConto, 2012) and deserves a separate discussion (see Subsection 3.5).

230 3.2. Boundary conditions

231 All the simulations are performed using a horizontal resolution of 20 km
232 on a regular rectangular grid covering the Eurasian domain (210×270 grid-
233 cells). Boundary conditions are regridded onto a Lambert Equal Area geo-
234 graphical projection centered on the North Pole (0°E , 90°N), and include:

- 235 • Pre-Industrial (1850 a.d., PI) surface topography and bedrock eleva-
236 tion, based on the International Bathymetric Chart of the Arctic Ocean
237 (IBCAO) dataset (Jakobsson, 2014);
- 238 • LGM surface topography, ice thickness and bedrock elevation, based
239 on the ICE-5G glacio-isostatic reconstruction (Peltier, 2004);
- 240 • Geothermal heat flux map from (Shapiro and Ritzwoller, 2004) and
241 sediment thickness map from (Laske, 1997).

242 The use of the ICE-5G reconstruction (Peltier, 2004) instead of more
243 recent glacio-isostatic reconstructions (*e.g.* ICE-6G (Peltier et al., 2015),
244 GLAC-1d (Tarasov et al., –)) ensure consistency between the LGM boundary
245 conditions and the climate forcing (see Subsections 3.3, 3.4.1). In fact, ICE-
246 5G surface topography, ice thickness and bedrock elevation are also used

247 in the LGM climate simulation used to force GRISLI (Braconnot et al.,
248 2012). Finally, during runtime the isostatic bedrock response to the ice load
249 is computed as a prognostic variable with the Elastic Lithosphere-Relaxed
250 Asthenosphere (ELRA) method (Le Meur and Huybrechts, 1996).

251 *3.3. Spin-up simulation setup*

252 In order to initialise the thermodynamical state of the ice sheet, we run a
253 100 kyrs-long transient spin-up simulation between 122 ky BP (MIS5e) and
254 the LGM. We assume that at MIS5 both topography and climatology were
255 close to PI conditions, similarly as in (Peyaud et al., 2007; Patton et al.,
256 2016). Therefore, at the beginning of the spin-up simulation we prescribe
257 the IBCAO (Jakobsson, 2014) PI bedrock elevation and the PI climatology
258 (30-years averaged annual/July mean air temperature and annual mean pre-
259 cipitation), simulated with the IPSL-CM5A-LR Atmosphere-Ocean General
260 Circulation Model (AOGCM, (Braconnot et al., 2012), fig.2). The PI cli-
261 mate fields are downscaled from the AOGCM global grid onto the ice sheet
262 model Eurasian grid using the IBCAO (Jakobsson, 2014) PI surface topogra-
263 phy. During the spin-up simulations, the climate forcing is progressed from
264 PI to LGM conditions by means of a normalized climate index based on the
265 NGRIP $\delta 18\text{O}$ record (Andersen et al., 2004). The LGM climatology (30-years
266 averaged annual/July mean air temperature and annual mean precipitation)
267 simulated with the same IPSL-CM5A-LR AOGCM (Braconnot et al., 2012)
268 (Fig. 2) is downscaled using the ICE-5G surface elevation (Peltier, 2004)
269 and prescribed for the last 1000 years of the simulation. During the spin-up
270 simulation, the sea level is progressed from 0 to -125 meters, using again a
271 normalized climate index based on the NGRIP $\delta 18\text{O}$ record (Andersen et al.,

272 2004). The sub-shelf melting is kept constant and equal to 0.1 m/yr, in order
 273 to allow the expansion of grounded ice over the Barents and Kara seafloors.
 274 Values of the main ice sheet model parameters in the spin-up simulation are
 275 listed in Table 1.

276 3.4. Transient simulations setup

277 3.4.1. Climate forcing

278 In all the transient simulations of the last deglaciation presented in this
 279 study, the downscaled LGM and PI climatology simulated with the IPSL-
 280 CM5A-LR AOGCM (Braconnot et al., 2012) (Fig. 2) are prescribed as initial
 281 and final climate snapshots, respectively. During runtime, the climatology
 282 is progressed from LGM to PI conditions using different indexes for annual
 283 mean temperature and precipitation (Fig. 3A). The indexes, which are taken
 284 as representative of three macro-regions (Fennoscandia, Svalbard/Barents
 285 Sea and Siberia/Kara Sea, see Supplementary Materials in (Petrini et al.,
 286 2018)), are derived from the non-accelerated transient climate simulation of
 287 the last 21 kyrs, TraCE21ka (Liu et al., 2009). Indices are normalized and
 288 vary between 1 and 0 for LGM and PI, respectively. The surface-elevation
 289 feedback is parametrised using the topographic lapse-rate (λ) and elevation-
 290 desertification (γ) factors, which correct the annual mean temperature and
 291 precipitation, respectively, for changes in elevation (Charbit et al., 2002;
 292 Marshall et al., 2007). At a given time-step t , the annual mean temperature
 293 and precipitation are then obtained as follows,

$$\begin{aligned}
 T_a(t) &= T_{\text{LGM}} \cdot i(t) + T_{\text{PI}} \cdot (1 - i(t)) - \lambda \cdot (s(t) - s_{\text{LGM}}), \\
 P_a(t) &= P_{\text{PI}} \cdot \left[\left(\frac{P_{\text{LGM}}}{P_{\text{PI}}} - 1 \right) \cdot i(t) + 1 \right] \cdot \exp(\gamma \lambda \cdot (s(t) - s_{\text{LGM}})),
 \end{aligned}
 \tag{10}$$

294 where i is one of the different climate indexes used in this study and s is the
295 surface elevation. The values of the topographic lapse-rate and elevation-
296 desert factors used in the transient simulations are not the same as in the
297 spin-up simulation and are discussed in Section 3.5. Our choice of using
298 the TraCE21ka simulation (Liu et al., 2009) to derive macro-regional climate
299 indexes only is motivated by the fact that the LGM climatology simulated
300 with the IPSL-CM5A-LR AOGCM (Braconnot et al., 2012) provided the best
301 fit between the simulated and reconstructed (Hughes et al., 2016) Eurasian
302 ice sheets at the LGM.

303 *3.4.2. Ocean forcing*

304 In all the transient simulations of the last deglaciation presented in this
305 study, we force the two-equation sub-shelf melting formulation (see Section
306 3.1) with four different time-varying vertical profiles of annual mean ocean
307 temperature and salinity, derived from the non-accelerated transient climate
308 simulation of the last 21 kyrs, TraCE21ka (Liu et al., 2009). Similarly as
309 for the atmospheric indexes, the ocean temperature and salinity vertical
310 profiles are taken as representative of four macro-regions (Norwegian Sea,
311 south-western and north-western Barents Sea and southern Arctic Ocean,
312 see Supplementary Materials in (Petrini et al., 2018)). Ocean vertical pro-
313 files representative of the south-western and north-western Barents Sea are
314 prescribed at the south-western and north-western ice sheet margins, respec-
315 tively, whereas at the northern margin of the ice sheet we force the sub-shelf
316 melting formulation with ocean vertical profiles representative of the south-
317 ern Arctic Ocean. Using these ocean temperature and salinity profiles, ocean
318 thermal forcings and basal melt rates are computed at each time step (Eqs.

319 7, 8, 9) at five different depth layers (-2 m, -200 m, -400 m, -600 m, -800 m)
320 and then vertically interpolated. Time-series of the ocean thermal forcing in
321 the Barents Sea (average between south-western and north-western sectors)
322 and southern Arctic Ocean at different depths are shown in Figure 3B. Fi-
323 nally, the sea level is progressed from -125 meters (LGM) to 0 meters (PI)
324 during runtime, using a normalized index based on the NGRIP $\delta^{18}\text{O}$ record
325 (Fig. 3A).

326 *3.5. Perturbed physics ensemble of transient ice sheet model simulations*

327 A large source of uncertainty in ice sheet model simulations is the pres-
328 ence of semi-empirical parametrisations in the models, whose parameters
329 spans a large range of values in the literature. In this study, instead of per-
330 forming a fine-tuning of individual parameters, we use the maxi-min Latin
331 Hypercube Sampling (mLHS) procedure to obtain random samples of $k = 5$
332 selected ice sheet model parameters. In this procedure, for each model pa-
333 rameter $n = 100$ values are randomly distributed in the intervals $(a, a + 1/n)$,
334 $(a + 1/n, a + 2/n), \dots, (b - 1/n, b)$, where a and b are the lower and upper
335 bounds, respectively, of the parameter range of values. Due to the large
336 uncertainties regarding the selected model parameters, the n values of each
337 parameter are chosen in such a way that the minimal distance among pairs
338 of points is maximized. The n values of k model parameters are then ran-
339 domly permuted, and the combinations of sampled parameters are used to
340 generate a perturbed physics ensemble of 100 transient simulations of the last
341 deglaciation. The ratio $n/k = 20$ between the number of simulations and
342 the selected model parameters is the same adopted by (Stone et al., 2010;
343 Applegate et al., 2015), whereas a larger number of model parameters and

344 simulations/parameters ratio were used by (Gregoire et al., 2016; Stokes and
345 Tarasov, 2010; Tarasov et al., 2012). Nevertheless, choosing $n/k = 20$ rep-
346 resents a reasonable tradeoff between minimizing the computing time and
347 sufficiently covering the parameter space (Stone et al., 2010).

348 Our choice of model parameters included in the statistical sampling is re-
349 lated to the main mechanisms of ice loss in a marine-based ice sheet. Ice flows
350 from the interior towards fast-flowing regions mainly due to internal defor-
351 mation. In this type of flow, commonly referred to as simple-shear flow, the
352 anisotropy of the ice plays an important role in determining the stress regime
353 (Ma et al., 2010). In GRISLI, the SIA enhancement factor E_{SIA} accounts for
354 the anisotropy of polycrystalline ice under condition of simple-shear flow (Ma
355 et al., 2010). Under higher values of E_{SIA} , the ice will deform more easily,
356 and the ice transport from the interior towards the fast-flowing regions will
357 be more efficient. Large-scale ice sheet modeling studies adopted a range
358 from 1 to 5 for this parameter (Stone et al., 2010; Applegate et al., 2015;
359 Colleoni et al., 2016). However, a higher value of 5.6 is suggested in a study
360 where an anisotropic full-Stokes model is used (Ma et al., 2010). Therefore,
361 in this study we select the range 1 – 5.6. In fast-flowing regions (*i.e.*, ice
362 streams), ice is rapidly delivered to the ice sheet margins, where mass loss
363 can occur by surface ablation, sub-shelf melting or calving. In GRISLI, the
364 flow regime in ice streams is simulated with the “dragging ice shelf” exten-
365 sion of the SSA. In these regions, the SSA is combined with a friction law,
366 $\tau_b = c_f N u_b$, where N is the effective pressure, u_b is the basal velocity and
367 c_f is the basal drag coefficient, which regulates the resistive force acting at
368 the ice stream base. Lower values of c_f leads to larger sliding velocities in

369 ice streams, thus increasing the ice transport towards the ice sheet edges.
370 This parameter was set in previous large-scale ice sheet modeling studies to
371 $1 \cdot 10^{-5}$ (Peyaud et al., 2007), $9 \cdot 10^{-5}$ (Dumas, 2002) and between $10 \cdot 10^{-5}$
372 and $100 \cdot 10^{-5}$ (Álvarez Solás et al., 2011). In this study, we explore the range
373 $1 \cdot 10^{-5} - 100 \cdot 10^{-5}$. Ice melting at the ice sheet margins is determined by
374 ablation and ocean melting under the ice shelves. When an ice sheet becomes
375 thinner, ablation zones can form or expand in response to increased air tem-
376 peratures due to surface elevation lowering. In this study, we parametrise this
377 positive feedback by means of the topographic lapse-rate λ , which represents
378 an approximation of how much the near-surface air temperature changes with
379 elevation. Previous large-scale ice sheet modeling studies adopted a range
380 for this parameter from 4 to $8.2^\circ\text{C}/\text{km}$ ((Stone et al., 2010; Gregoire et al.,
381 2016; Colleoni et al., 2016), whereas climate simulations suggest a range from
382 4 to $7^\circ\text{C}/\text{km}$ (Abe-Ouchi et al., 2007). In this study, we explore the range
383 $4 - 8.2^\circ\text{C}/\text{km}$. The increase in air temperatures caused by surface elevation
384 lowering will also results in an increase in precipitation, due to the larger
385 saturation pressure of water vapour. This negative feedback, which can par-
386 tially compensate for the increase in ablation, is represented in this study via
387 the elevation-desertification factor γ . Large-scale ice sheet modeling studies
388 suggest a range between 0.03 and 0.078°C^{-1} for this parameter (e.g., (Char-
389 bit et al., 2002)), whereas climate modelling studies suggest that γ can take
390 higher values up to 0.11°C^{-1} ((Colleoni et al., 2016) and references therein).
391 In this study, the range $0.03 - 0.1^\circ\text{C}^{-1}$ is explored. Finally, in the sub-shelf
392 melting formulation used in this study the magnitude of melting rates in re-
393 sponse to the ocean thermal forcing (see Eq. 7) is modulated by the sub-shelf

394 melting parameter F_m . This dimensionless parameter has been previously in-
395 troduced in order to match simulated and observed grounding-line position
396 in Antarctica (Pollard and DeConto, 2012; Martin et al., 2011). However,
397 the oceanic conditions used in (Pollard and DeConto, 2012; Martin et al.,
398 2011) to force the sub-shelf melting parametrisation are drastically different
399 from those used in this study (Fig. 4). Therefore, we identify a new range
400 of values for F_m so that the sub-shelf melting rates are within the range of
401 values observed under the present-day Antarctica ice shelves (Rignot et al.,
402 2013; Paolo et al., 2015; Pritchard et al., 2012) (see Supplementary Materi-
403 als in (Petrini et al., 2018)). The range of values explored in this study is
404 $0.005 \cdot 10^{-3} - 1.5 \cdot 10^{-3}$. The list of GRISLI model parameters included in
405 the mLHS in this study, with their associated range of values, is summarised
406 in Table 2.

407 Our list of model parameters is slightly different from that used by (Stone
408 et al., 2010; Applegate et al., 2015; Gregoire et al., 2016), where ice/snow
409 melt factors and the geothermal heat flux were included in the statistical
410 sampling. In this study, we do not consider these parameters in the sampling
411 as they are not single-valued, with melt factors depending on the July mean
412 air temperature and the geothermal heat flux being prescribed from a two-
413 dimensional map (see Subsection 3.1).

414 *3.6. Model-data comparison*

415 In order to rule out unrealistic simulations, we test each member of the
416 ensemble of 100 transient simulations of the last deglaciation against the
417 data-based deglacial chronologies from the DATED-1 archive (Hughes et al.,
418 2016). The DATED-1 archive (Hughes et al., 2016) provides time-slice most-

419 credible, minimum and maximum (mc, min and max, respectively) recon-
 420 structions of the Eurasian ice sheets extent between 21 and 10 ky BP. Such
 421 reconstructions are based on a comprehensive collection of existing pub-
 422 lished chronological data with a census date of 1 January 2013. In the
 423 BSIS region, radiocarbon dates based on marine cores from the continen-
 424 tal shelf and trough-mouth fans on the continental slope are combined with
 425 generalized flow patterns to reconstruct the ice sheet retreat pattern and
 426 configuration. In order to provide a quantitative comparison between the
 427 simulated and reconstructed deglaciation scenarios, all the DATED-1 recon-
 428 structions between 21 and 13 ky BP are regridded onto the ice sheet model
 429 grid. For each ensemble member, at each time slice we compute the per-
 430 centage of the “total” BSIS area showing model/data agreement, overesti-
 431 mation and underestimation (Fig. 4B). The “total” BSIS area is defined as
 432 $A_{TOT}=(A_s \cap A_D)\cup(A_s \setminus A_D)\cup(A_D \setminus A_s)$, where A_s is the simulated area and
 433 A_D is the DATED-1 area. At each time slice, a grid cell is considered to show
 434 model/data agreement if there is agreement between the simulated scenario
 435 and at least one of the DATED-1 scenarios (mc-min-max). Otherwise, the
 436 model overestimates or underestimates the ice extent in that specific gridcell
 437 compared to the DATED-1 reconstruction. For our final analysis, we se-
 438 lect a restricted group of nine ensemble members (“admissible simulations”)
 439 showing the largest percentage of total ice sheet area model/data agreement
 440 (Fig. 4B). These nine ensemble members satisfies the following minimal re-
 441 quirements of model-data agreement: (a) 21-13 ky BP average model/data
 442 agreement larger than 60% (b) minimum time slice model/data agreement
 443 larger than 40% (c) last time slice (13 ky BP) model/data agreement larger

444 than 50%. These model/data agreement percentages are relatively low as in
445 all the ensemble members the ice sheet extent at the eastern margin is system-
446 atically overestimated (Fig. 4A). In Subsection 4.2.2 this large model/data
447 mismatch is carefully analyzed, and several hypothesis to explain the over-
448 estimation are proposed. In the western, central and northern Barents Sea
449 the ice sheet extent throughout the deglaciation has a much larger variability
450 across the ensemble, and the admissible simulations provide the best fit with
451 the DATED-1 reconstruction (Fig. 4A). The range of values assumed by the
452 model parameters c_f , λ and γ in the admissible simulations remains similar
453 to the full range of values considered for the mLHS procedure, with individ-
454 ual values spreading across the full interval length (Fig. 5 and Table 2). In
455 contrast, the values assumed by parameters E_{SIA} and F_m in the admissible
456 simulations are more clustered in the second half of the full range interval
457 (Fig. 5 and Table 2).

458 The nine admissible simulations are used to construct minimum (min),
459 maximum (mc) and average (avg) simulated deglaciation scenarios every
460 thousand years between 21 and 13 ky BP. In the next section, these sce-
461 narios are analyzed and compared with the DATED-1 min-max-mc recon-
462 structions. In the comparison between min-max-avg simulated scenarios and
463 the DATED-1 min-max-mc reconstructions, a grid cell is considered to show
464 agreement between model and observations if there is agreement between at
465 least one of the three simulated/DATED-1 scenarios. Otherwise, the simu-
466 lated ice extent is either overestimated/underestimated in that specific grid-
467 cell compared to the DATED-1 reconstruction.

Symbol	Description	Units	Value
E_{SIA}^*	SIA enhancement factor	-	3
E_{SSA}	SSA enhancement factor	-	1
c_f^*	Basal drag coefficient	-	$2 \cdot 10^{-5}$
c_i	Ice heat capacity	J/kg°C	2009
κ_i	Ice thermal conductivity	J/m°Cs	2.1
λ^*	Lapse-rate value	°C/km	0.005
γ^*	Precipitation-correction factor	1/°C	0.05
ρ	Ice density	kg/m ³	917
K	Hydraulic conductivity	m/s	10^{-6}
H_c	Thickness threshold for the calving criterion	m	200
τ_f	Relaxation time of the asthenosphere	yr	3000
f_m^*	Sub-shelf melting parameter	-	-
b_m	Sub-shelf melting rate	m/yr	0.1

Table 1: List of GRISLI model parameters. The parameters marked with a star refer to the spin-up simulation only, whereas their range of values in the transient simulations of the last deglaciation is listed in Table 2.

468

Symbol	“FE” Range	“FE” Avg	“AS” range	“AS” avg
λ	[4 – 8.2]	6.1	[5.0 – 7.8]	6.5
γ	[0.03 – 0.1]	0.065	[0.05 – 0.1]	0.082
E_{SIA}	[1 – 5.6]	3.3	[3.6 – 5.4]	4.8
c_f	$[1 – 10] \cdot 10^{-5}$	$5 \cdot 10^{-5}$	$[2 – 10] \cdot 10^{-5}$	$4 \cdot 10^{-5}$
f_m	$[0.005 – 1.5] \cdot 10^{-3}$	$0.8 \cdot 10^{-3}$	$[0.6 – 1.5] \cdot 10^{-3}$	$1.2 \cdot 10^{-3}$

Continued on the next page

Continued from previous page

Symbol	“FE” Range	“FE” Avg	“AS range	“AS” avg
--------	------------	----------	-----------	----------

Table 2: List of GRISLI model parameters included in the mLHS, with their associated “Full Ensemble”/“Admissible Simulations” range of values (“FE” Range/“AS” range) and average value (“FE” avg/“AS” avg).

469

470 4. Results and discussion

471 4.1. Barents Sea Ice Sheet during the LGM

472 At the end of the spin-up simulation, Northern Eurasia is covered by an
473 interconnected complex of ice sheets (Fig. 6A). The BSIS is connected to
474 the SIS in the south and covers a total area of 2.42 Mkm² (Fig. 6A, 7B and
475 Table 3). The western and northern margins of ice sheet extend up to to the
476 continental shelf break in the western and northern Barents Sea, respectively,
477 whereas the eastern termination of the ice sheet is located in the relatively
478 shallow central Kara Sea (Fig. 1, 6A).

479 The simulated ice sheet extent is slightly underestimated (3% of the total
480 area) with respect to the DATED-1 reconstruction (Fig. 10 and 4). The sim-
481 ulated grounding-line position is slightly shifted towards the interior of the ice
482 sheet at the mouth of Kvitøya, Franz Victoria, St. Anna and Bjørnøyrenna
483 ice streams. This underestimation can be explained by looking at the mass
484 budget at the ice sheet western and northern margins during the LGM. The
485 July mean air temperature remains below -5 °C in the region covered by the
486 BSIS (Fig. 2), thus preventing the formation of ablation zones. The sub-shelf

487 melting is set to a constant, low value of 0.1 m yr^{-1} and the mean annual
488 precipitation is lower than 0.3 m yr^{-1} . Therefore, the mass budget over the
489 floating ice shelves at the ice streams mouth is either slightly positive or neg-
490 ative and prevents the floating ice proximal to the grounding-line to thicken
491 enough to become grounded (see Fig. 6A, 6B). In addition, the eustatic sea
492 level prescribed at the LGM (-125 meters) does not account for spatial vari-
493 ability in relative sea level. A lower relative sea level at the mouth of Kvitøya,
494 Franz Victoria, St. Anna troughs and Bjørnøyrenna would therefore allow
495 the ice stream front to extend up to the continental shelf edge.

496 The simulated ice sheet extent overestimation relative to DATED-1 is
497 the 12% of the total ice sheet area, mainly due to an excess of ice covering
498 Severnaya Zemlya and impinging onto Taimyr Peninsula at the north-eastern
499 margin (Fig. 1, Fig. 10 and 4). The presence of this overestimated ice lobe is
500 strictly linked with the LGM temperature and precipitation simulated with
501 the IPSL-CM5A-LR AOGCM (Braconnot et al., 2012) (Fig. 2). Although
502 the annual mean precipitation is relatively low in this area, ranging between
503 0.1 and 0.3 m yr^{-1} , the annual surface mass balance remains positive as July
504 mean air temperatures remain below -5°C , thus preventing summer ablation.
505 It is interesting to note that in the immediate vicinity of the north-eastern
506 and eastern ice sheet margin, July mean air temperatures are above zero and
507 range from 0 to 5°C (Fig. 2). Therefore, we claim that the negative LGM
508 July mean air temperature simulated with the IPSL-CM5A-LR AOGCM
509 (Braconnot et al., 2012) over the north-eastern ice sheet margin are caused
510 by the use of the ICE-5G (Peltier, 2004) LGM ice sheet extent/thickness in
511 the climate model. In fact, also in the ICE-5G reconstruction an ice lobe more

512 than 800 meters thick is covering Severnaya Zemlya and the coast of Taimyr
513 Peninsula, thus largely overestimating the surface topography in this area
514 with respect to what recent reconstructions suggest (Hughes et al., 2016).
515 The ice extent overestimation at the LGM is also observed in both ICE-6G
516 (Peltier et al., 2015) and GLAC-1d (Tarasov et al., –) glacio-isostatic recon-
517 structions, and currently there are no published reconstructions based on
518 GIA models correcting the ice sheet extent in the north-east. The boundary
519 between strong negative (less than -5°C) and positive July mean air tempera-
520 tures matches exactly the ICE-5G ice sheet eastern limit (Fig. 2), suggesting
521 that also at the eastern margin the ICE-5G ice thickness may play a role
522 in overestimating the LGM cooling in the climate model (Braconnot et al.,
523 2012). Looking at the simulated LGM annual mean air temperatures (Bra-
524 connot et al., 2012), a cooling between -10 and -20°C is observed with respect
525 to PI (Fig. 2) at the north-eastern and eastern ice sheet margins. Pollen-
526 based reconstructions from the North Siberian Lowland suggest a lower LGM
527 cooling ranging between -4 and -10°C (Bartlein et al., 2011) (Fig. 2). Outside
528 the ice sheet eastern and north-eastern margins the LGM-PI annual mean
529 air temperature cooling simulated with the IPSL-CM5A-LR climate model
530 (Braconnot et al., 2012) has a similar range compared to proxy reconstruc-
531 tion (Fig. 2). Finally, previous modelling studies showed that the PDD
532 method tends to underestimate surface ablation (Sergienko and Macayeal,
533 2005; Pritchard et al., 2008). Therefore, the impact of a cold bias at the
534 north-eastern and eastern ice sheet margins during the LGM could be possi-
535 bly amplified by the simplified method used in this study to compute surface
536 ablation.

537 *4.2. Last deglaciation of the BSIS*

538 *4.2.1. Early western margin retreat between 21 and 18 ky BP*

539 Between 21 and 19 ky BP, the BSIS loses around 0.34 Mkm^2 of ice cover
540 at a rate between 150 and $180 \text{ km}^2/\text{yr}$ (Fig. 7 and Table 3). More than a half
541 of this initial area loss is due to the simulated retreat of the Bjørnøyrenna
542 ice stream at the western ice sheet margin, which register an area loss of
543 0.23 Mkm^2 (Fig. 8 and Table 3). Between 21 and 20 ky BP, the ice stream
544 front retreats from the outer to the central trough, and by 19 ky BP the
545 central branch of Bjørnøyrenna ice stream reaches the outer part of Sentral-
546 bankrenna (Fig. 9). Between 19 and 18 ky BP, the ice sheet loses 0.15 Mkm^2
547 of ice cover, at a rate of $150 \text{ km}^2/\text{yr}$ (Fig. 7 and Table 3). The western ice
548 sheet margin show an area loss of 0.11 Mkm^2 (Fig. 8 and Table 3), with
549 the Bjørnøyrenna ice stream further retreating towards the inner part of the
550 trough (Fig. 9). Between 20 and 18 ky BP, the simulated grounding-line
551 position at the mouth of Bjørnøyrenna ice stream is shifted up to 50 km
552 towards the inner/outer part of the trough in the minimum/maximum sim-
553 ulated scenarios, respectively (Fig. 9). At the northern ice sheet margin, in
554 all three simulated scenarios the Kvitøya, Franz Victoria, Voronin and St.
555 Anna ice streams show a limited retreat during this initial phase (Fig. 9).
556 The overall area loss at the northern ice sheet margin is 0.1 Mkm^2 in three
557 thousand years, with relatively low retreat rates ranging between 40 and 50
558 km^2/yr (Fig. 8 and Table 3).

559 The relatively low simulated retreat of the ice streams at the northern
560 ice sheet margin cannot be directly linked to climatic factors, as between 21
561 and 15 ky BP the SMB remains positive and the sub-shelf melting is close

562 to zero (Fig. 9). In fact, during this time interval annual and July mean air
563 temperatures over the Barents and Kara seas remain at their LGM values,
564 and the Arctic Ocean thermal forcing is close to zero (Fig. 3A, B). Therefore,
565 this slow, steady retreat can only be explained by an unstable response of
566 the ice streams to the initial sea level rise prescribed after the LGM. Inside
567 the deep, retrograde-sloping troughs at the northern ice sheet margin, the
568 ice thickness at the grounding-line is close to its flotation threshold during
569 the LGM (see Fig. 6A, 6C). The sea level increase prescribed after 21 ky BP
570 causes grounded ice to become afloat and accelerate, as a result of the sudden
571 lack of basal drag. This can lead to a further increase in the longitudinal
572 stresses upstream, causing in turn further thinning at the grounding-line,
573 which already migrated inland where the trough is deeper. However, this
574 process is not irreversible and is stopped when the grounding-line retreats
575 inland into a region with higher ice thickness, well above the flotation thresh-
576 old. For this reason, the simulated retreat of the northern margin ice streams
577 between 21 and 18 ky BP is relatively slow and only cause the grounding-line
578 to recede from the outer into the inner troughs. Both observations and ice
579 sheet modelling studies showed that sea level rise alone is capable of initiating
580 relatively slow, episodic ice retreat events (Mackintosh et al., 2011; Cofaigh
581 et al., 2019).

582 The initial simulated retreat of Bjørnøyrenna ice stream is much larger
583 than those simulated at the northern ice sheet margin and therefore cannot
584 be explained by sea level rise alone. Even though both the western and
585 northern margins share a similar, positive SMB (Fig. 8), the oceanic forcing
586 at the two margins are drastically different (Fig. 3B). Between 21 and 19

587 ky BP, the ice loss at the western margin due to sub-shelf melting rapidly
588 increase, reaching values of 76 Gt/yr (Fig. 8 and Table 3). This increase
589 can be explained by the relatively high ocean thermal forcing prescribed
590 between 200 and 400 meters depth, due to the presence of warm subsurface
591 Atlantic water (Fig. 3B). Even though this warm ocean layer does not fully
592 reach grounding-line depths within the trough (Fig. 1), it is deep enough to
593 cause prolonged ice shelf thinning and grounding-line retreat. Between 19
594 and 17 ky BP, the integrated ice loss at the western ice sheet margin due to
595 sub-shelf melting slightly decreases, in spite of the increase in ice shelf area
596 (Fig. 8 and Table 3). This can be explained by a reduction in the ocean
597 thermal forcing prescribed at 400 and, to a less extent, at 200 meters depth
598 (Fig. 3B) due to the AMOC gradual weakening in the TraCE21ka simulation
599 (Liu et al., 2009). This decrease in sub-shelf melting at the western margin
600 corresponds to a slowdown in the rate of ice area loss (Fig. 8 and Table 3),
601 thus suggesting that the oceanic forcing played a primary role in modulating
602 the initial retreat of the western ice sheet margin.

603 The early simulated retreat of the Bjørnøyrenna ice stream and, to a less
604 extent, of other major ice streams (Kvitøya, Franz Victoria and St. Anna) at
605 the northern ice sheet margin is larger than in the DATED-1 min-mc-max sce-
606 narios, leading to an increase in the ice area underestimation up to 0.2 Mkm²
607 (8-10% of the total ice sheet area, Fig. 10 and Table 4). In the DATED-1
608 reconstruction, the Kvitøya, Franz Victoria and St. Anna ice streams front
609 position remains unchanged until 19 ky BP. By this time, the simulated ice
610 streams at the northern ice sheet margin already started to slowly, steadily
611 retreat (Fig. 10). After 19 ky BP, the DATED-1 reconstruction suggests

612 that the ice streams at the northern ice sheet margin started to retreat into
613 the inner trough, and from 17 ky BP onwards the simulated and DATED-1
614 northern margin extent are in good agreement (Fig. 10). In the DATED-1
615 scenarios, the Bjørnøyrenna ice stream does not retreat significantly from
616 the continental shelf edge between 21 and 19 ky BP. Only during the fol-
617 lowing two thousand years the southern branch of the ice stream recedes in
618 the inner part of Bjørnøyrenna. The mismatch between the simulated and
619 reconstructed Bjørnøyrenna ice stream front position is already large at 20
620 ky BP and peaks at 18 ky BP (Fig. 10 and Table 4).

621 The model-data mismatch at the western and northern ice sheet mar-
622 gin between 21 and 18 ky BP can be explained by several factors. First,
623 the coarse horizontal resolution (20 km) used in this study might amplify
624 the grounding-line response to both ice shelf thinning and increase in the
625 prescribed sea level. Moreover, the size of the simulated Bjørnøyrenna ice
626 stream during the LGM (Fig. 6B) is larger, especially in the south, than
627 what marine geophysical data suggest (Andreassen and Winsborrow, 2009;
628 Bjarnadóttir et al., 2014; Piasecka et al., 2016; Esteves et al., 2017; New-
629 ton et al., 2017). In this regard, the method used in GRISLI to identify
630 ice stream areas (presence of thick sediment layers saturated by meltwater
631 (Peyaud et al., 2007)) and to parametrise subglacial hydrology (based on
632 a simple hydraulic gradient model (Peyaud et al., 2007)) might favor the
633 formation of large ice streams in topographic depressions. An overestima-
634 tion of the Bjørnøyrenna ice stream area can amplify the fast and unstable
635 response to ice shelf thinning and sea level rise, although it is difficult to
636 properly quantify such an amplification. Another factor is related to the

637 TraCE21ka ocean forcing prescribed at the western Barents Sea margin be-
638 tween 21 and 18 ky BP (Supplementary Fig. S1). During this time interval,
639 subsurface (200-400 meters depth) ocean annual mean temperatures range
640 between 2 and 4 °C. The presence of relatively warm and saline subsurface
641 Atlantic water at the western and north-western Barents Sea margins dur-
642 ing the LGM has been detected in sediment cores (Chauhan et al., 2014,
643 2016), suggesting mean summer SST values between 1 and 3 °C (Nørgaard-
644 Pedersen et al., 2003; Pflaumann et al., 2003). However, these values might
645 be overestimated up to 3 °C, due to well-known biases in the methodology
646 used to reconstruct the SSTs from the paleoenvironmental proxies (Sarnthein
647 et al., 2003). Therefore, we cannot exclude an overestimation of the western
648 Barents Sea subsurface ocean forcing prescribed between 21 and 18 ky BP.
649 We also highlight that the relatively simple sub-shelf melting parametrisa-
650 tion used in this study, accounting for ice-ocean heat exchanges only, could
651 potentially amplify the effect of such an overestimation. The ocean tempera-
652 ture profiles prescribed at the western Barents Sea between 21 and 18 ky BP
653 present a relatively warm subsurface layer (200-400 meters depth) and sub-
654 zero temperatures below 400 meters depth (Supplementary Fig. S1). The
655 LGM bedrock elevation in Bjørnøyrenna is mostly deeper than 400 meters
656 (Fig. 1), implying that sub-shelf melting rates will be systematically lower
657 close to the grounding-line and higher towards to the shelf edge. This is
658 in contradiction with sub-shelf melting rates calculated over the Antarctic
659 ice shelves with more refined methods such as ocean cavity circulation and
660 plume models (Lazeroms et al., 2018; Reese et al., 2018; Pelle et al., 2019). In
661 these studies, higher melt rates are simulated close to the grounding-line, and

662 lower values, possibly negative, are found as the distance from the grounding-
663 line increases, due to the cooling effect of buoyant melt-water plumes rising
664 along the shelf base towards the calving front. However, after 18 ky BP the
665 ocean temperature profiles used to force the sub-shelf melting formulation
666 show lower temperatures in the first 400 meters and higher temperatures
667 below (Supplementary Fig. S1). These types of ocean profiles are more
668 similar to those used in (Favier et al., 2019) to assess the good agreement
669 of the sub-shelf melting formulation used in this study with coupled ocean-
670 ice sheet simulations under idealised ocean warming scenarios. Therefore,
671 we expect that the overestimation of sub-shelf melting rates away from the
672 grounding-line did not occur after 18 ky BP, and more realistic sub-shelf
673 melting patterns were simulated.

674 *4.2.2. Late retreat of the eastern margin*

675 Between 21 and 19 ky BP, the north-eastern and eastern margins of the
676 ice sheet remain mostly unchanged in both the simulated and DATED-1
677 scenarios (Fig. 10). However, between 19 and 18 ky BP, the DATED-1
678 reconstruction suggests an abrupt retreat of the eastern ice sheet margin,
679 reaching west of Novaya Zemlya towards the central Barents Sea. This retreat
680 in the DATED-1 reconstruction continues, although at lower rates, in the
681 following two thousand years, leaving St. Anna Trough ice-free by 17 ky
682 BP and presenting at 16 ky BP an eastern margin well established in the
683 central Barents Sea (Fig. 10). In all the simulated scenarios (min-avg-max)
684 the eastern and north-eastern ice sheet margins show a drastically different
685 behaviour, with the margin position not showing significant changes between
686 21 and 15 ky BP (Fig. 9, 10). This leads to an increase in the overestimated

687 ice area up to 0.6 Mkm^2 (25-35% of the total area, Fig. 10 and Table 4).

688 The stable behaviour of the simulated eastern margin can be explained
689 by looking at the atmospheric and oceanic conditions. First, the annual and
690 July mean temperatures over Siberia and Kara Sea remains nearly constant
691 at their LGM value until around 17 ky BP, and are still close to this value
692 at 16 ky BP (Fig. 3A). Moreover, the ocean water still does not have access
693 to the simulated eastern and north-eastern ice sheet margins at 16 ky BP, as
694 the north-eastern ice lobe is still grounded on the coast of Taymir Peninsula
695 (Fig. 9). However, even if the connection with the Arctic ocean was open,
696 the TraCE21ka Arctic Ocean temperature profile shows temperatures lower
697 than $-1 \text{ }^\circ\text{C}$ throughout the water column until 16 ky BP (Supplementary Fig.
698 S1), and the corresponding thermal forcing remains very close to zero until
699 that time (Fig. 3B).

700 Proxies for summer SST and perennial sea ice cover (Nørgaard-Pedersen
701 et al., 2003; Pflaumann et al., 2003; De Vernal et al., 2005) suggest that
702 unlikely relatively warm subsurface Atlantic water could extend up to the
703 easternmost part of the northern margin and trigger a large, sustained margin
704 retreat as those suggested in the DATED-1 reconstruction. Moreover, even
705 if this was the case, the subsurface Atlantic water would have also fringed
706 the western and the westernmost part of the northern margin, thus triggering
707 margin retreats at least comparable to those occurring at the eastern margin.
708 This is not the case in the DATED-1 reconstruction, where the eastern ice
709 sheet margin starts to retreat earlier than the western and northern margins.
710 Even though the cold bias in the prescribed LGM climatology at the north-
711 eastern and eastern margins of the ice sheet (see Subsection 4.1) could be a

712 cause for the model/data mismatch, we find arguable that an increase in SMB
713 alone due to regional warming would be capable of driving such a rapid ice
714 sheet retreat. In view of this, we find unlikely that the model/data mismatch
715 at the eastern ice sheet margin was entirely caused by bias in the climate
716 forcings. A recent study combining a variety of marine proxies suggested
717 that a combination of glacio-isostatic depression and high relative sea level
718 initiated the last deglaciation of a marine-based sector of the BIIS, in absence
719 of ocean warming and when eustatic sea level was at the LGM minimum
720 (Cofaigh et al., 2019). A similar process could explain both the early retreat
721 of the eastern ice sheet margin and the model/data mismatch, as this study
722 only accounts for variations in eustatic sea level. Finally, it is highlighted
723 that the glacial evolution of the eastern ice sheet margin remains poorly
724 understood due to the limited amount of in-situ data available, as largely
725 discussed in (Hughes et al., 2016), and the DATED-1 margin positions in the
726 vicinity of Novaya Zemlya during and after the LGM are highly uncertain.
727 It cannot be therefore excluded that the model-data mismatch observed in
728 this region might be overestimated, and a relatively slow, steady retreat took
729 place at the eastern margin of the ice sheet between 19 and 16 ky BP.

730 *4.2.3. Collapse of the BSIS-SIS junction in the central Barents Sea*

731 After the slowdown in ice retreat between 19 and 17 ky BP, the rate of
732 ice area loss increase again, reaching $180 \text{ km}^2/\text{yr}$ at 16 ky BP and leading to
733 an ice area loss of 0.17 Mkm^2 between 17 and 16 ky BP (Fig. 7 and Table
734 3). In the following thousand years, the rate of ice area loss peaks to 390
735 km^2/yr , the higher values registered since the beginning of the deglaciation,
736 and the ice sheet lose 0.4 Mkm^2 of ice cover (Fig. 7 and Table 3). The area

737 loss during this time interval is mainly occurring in the central Barents Sea
738 (Fig. 8 and Table 3), which by 15 ky BP remains largely ice-free after the
739 disconnection between the BSIS and the SIS in the average and maximum
740 simulated scenarios (Fig. 9). In the minimum simulated scenario, the con-
741 nection between the BSIS and the SIS is already relatively thin at 17 ky
742 BP, and by 16 ky BP the ice sheets are already disconnected (Fig. 9). The
743 southern branch of Bjørnøyrenna ice stream is deglaciated at 15 ky BP in
744 all the simulated scenarios, whereas the northern branch of the ice stream
745 occupies the inner part of Persey Trough in the northern Barents Sea both
746 in the average and maximum simulated scenarios (Fig. 10). The area loss
747 at the northern margin between 17 and 15 ky BP remains lower than 0.1
748 Mkm², with an average retreat rate of 25 km²/yr (Fig. 8 and Table 3).

749 Once again, the simulated retreat of the western ice sheet margin ap-
750 pears to be primarily driven by the prescribed ocean conditions rather than
751 by SMB or sea level rise. In fact, during this time interval the integrated
752 SMB remains positive and the prescribed sea level remains nearly constant,
753 whereas the ice loss due to sub-shelf melting increase to 95 Gt/yr (Fig. 8
754 and Table 3). The increment of ice loss due to sub-shelf melting is caused
755 by a relatively low increase in the ocean thermal forcing prescribed at the
756 western Barents Sea margin below 200 meters depth (Fig. 3A) due to the
757 slow, gradual AMOC recovery in the TraCE21ka simulation between 17 and
758 15 ky BP, triggered by reduced Northern Hemisphere freshwater fluxes (Liu
759 et al., 2009). Even though the decrease in sedimentary Pa/Th ratio (a proxy
760 for AMOC strength) in a sediment core from Barbados seems to support this
761 hypothesis (McManus et al., 2004), a more recent analysis of the Pa/Th ratio

762 in a compilation of sediment cores from the Atlantic Ocean suggests that the
763 AMOC was still weak until around 15 ky BP (Ng et al., 2018). However, the
764 simulated AMOC in the TraCE21ka simulation is also weak between 17 and
765 15 ky BP and, despite its gradual increase during this time interval, the max-
766 imum AMOC transport does not exceed 5 Sv (Liu et al., 2009). Even though
767 Pa/Th ratio represents a good proxy for ocean circulation, it cannot reliably
768 quantify rates of AMOC weakening (Ivanovic et al., 2018). Therefore, it re-
769 mains difficult to conclude whether the ocean thermal forcing prescribed at
770 the western Barents Sea between 17 and 15 ky BP is overestimated.

771 The simulated and DATED-1 scenarios are in good agreement on the
772 timing of the disintegration of the junction between the BSIS and the SIS,
773 occurring between 17 and 16 ky BP in the minimum simulated and recon-
774 structed scenario and between 16 and 15 ky BP in the simulated average and
775 maximum scenarios and in the most-credible and maximum DATED-1 recon-
776 structions (Hughes et al., 2016) (Fig. 9). In both reconstructed and simulated
777 scenario, by 15 ky BP the southern margin of the BSIS has retreated north
778 in the central Barents Sea, and the ice sheet presents a continuous ice cover
779 from Svalbard in the north-west to Franz Josef Land (DATED-1 scenario)
780 and Novaya and Severnaya Zemlya (simulated scenario) in the north-east
781 (see for instance Fig. 10).

782 *4.2.4. Final ice sheet deglaciation in the Barents and Kara seas*

783 Between 15 and 14 ky BP, the simulated ice sheet experiences a further
784 increase in the rate of area loss ($690 \text{ km}^2/\text{yr}$ at 14.4 ky BP), losing 0.59 Mkm^2
785 of ice cover (Fig. 7 and Table 3). This major simulated area loss is due to
786 the final ice sheet deglaciation, with the Barents and Kara seas remaining

787 largely ice-free at 13 ky BP in all three simulated scenarios (Fig. 10). All
788 the major troughs at the northern ice sheet margin are already deglaciated
789 at 14 ky BP in the minimum and average scenarios, with the exception of
790 the inner part of St. Anna Trough (Fig. 10). However, by 13 ky BP all the
791 troughs are ice-free independently on the selected scenario, and the Kara Sea
792 is entirely ice-free in the average and minimum simulated scenario, whereas
793 an interconnected marine-based ice body joining Severnaya Zemlya and the
794 Taimyr Peninsula is still present in the maximum scenario (Fig. 10).

795 The ice sheet retreat between 15 and 14 ky BP is driven by a combination
796 of sub-shelf melting and abrupt sea level rise prescribed between 14.6 and
797 14.4 ky BP (Fig. 7, 8). In fact, during this time interval the ocean thermal
798 forcing below 200 meters keeps increasing in the Barents Sea and also starts to
799 increase in the Arctic Ocean (Fig. 3A), due to the abrupt AMOC overshoot
800 (*i.e.*, recovery past its LGM level) during the Bølling-Allerød event simulated
801 in TraCE21ka (Liu et al., 2009) (Fig. 3B). The sharp decrease in the Pa/Th
802 ratio in sediment cores from Barbados and the Atlantic Ocean seems to
803 support the relatively high AMOC export simulated in TraCE21ka during
804 this short-lived event (McManus et al., 2004; Ng et al., 2018), with relatively
805 warm, saline Atlantic water reaching for the first time the Arctic ocean at
806 the northern margin of the Eurasian basin (Supplementary Fig. S1). The
807 abrupt, short-lived jump in prescribed sea level rise causes a rapid increase
808 in the ice shelf area that, in combination with the ocean forcing, leads to
809 peaks in ice loss due to sub-shelf melting around 450 Gt/yr and 255 Gt/yr at
810 the southern and northern ice sheet margins, respectively (Fig. 8 and Table
811 3). After 14 ky BP, the prescribed sea level drops, but the sub-shelf melting

812 remains negative, in spite of its decrease due to the reduction in ice shelf area,
813 and leads to the final ice sheet collapse in the northern Barents Sea (Fig. 8
814 and Table 3). It is interesting to note how during the Bølling-Allerød event
815 the SMB not only does not become negative, but also increases. In fact, by
816 the onset of Bølling-Allerød the ice sheet has already retreated sufficiently
817 north in the Barents Sea (Fig. 8), where the PI July mean air temperatures
818 simulated with the IPSL-CM5A-LR AOGCM (Braconnot et al., 2012) are
819 below zero (Fig. 2). The combination of sub-zero summer temperatures and
820 increased snowfall (Fig. 3A) results in the SMB increase between 15 and 14
821 ky BP.

822 The simulated scenario is in agreement with the DATED-1 reconstruction
823 on the timing of the deglaciation in the northern Barents Sea, remaining
824 mostly ice-free at 13 ky BP (Fig. 10). By this time, both the simulated and
825 DATED-1 scenarios show isolated ice cover above sea level in Svalbard, Franz
826 Josef Land and Novaya Zemlya, whereas emerged lands in Severnalya Zemlya
827 and south of Storfjordren Trough are ice-covered in the simulated scenarios
828 only (Fig. 10).

829 *4.3. Drivers of ice retreat and insights on the long-term stability of the WAIS*

830 Overall, the simulated deglacial evolution of the BSIS presents a clear
831 south-west to north-east deglaciation pattern (Fig. 8, 9, 11) which reflects
832 well the differences in the TraCE21ka ocean forcing prescribed at the western
833 and northern ice sheet margins. Even though changes in eustatic sea level
834 do affect the grounding-line position, the magnitude of their impact appears
835 largely dependent on the oceanic background. This is clearly shown by the
836 simulated ice retreat at the northern ice sheet margin until 15 ky BP, where

837 in absence of sub-shelf melting rates of sea level rise and area loss are up
838 to 5 times lower than at the western margin (Table 3). Also the different
839 magnitude and timing of the peaks in sub-shelf melting at the western and
840 northern margins in response to the 14.6-14.4 ky BP abrupt eustatic sea
841 level rise indicate that changes in eustatic sea level amplified the effects of
842 ocean warming, rather than driving the ice retreat (Fig. 8 and Table 3).
843 Considering that the SMB remains positive throughout the deglaciation (Fig.
844 8) we can identify the ocean forcing as the primary driver of the simulated
845 last deglaciation of the BSIS. The strong impact of sub-shelf melting on
846 the evolution of marine-based ice sheets on multi-millennial timescales, as
847 opposed to the minor role played by atmospheric forcing and sea level rise,
848 has also been demonstrated in recent ice sheet modelling studies focusing on
849 the Eurasian ice sheets (Alvarez-Solas et al., 2019) and on the Antarctic Ice
850 Sheet (Mackintosh et al., 2011; Lowry et al., 2019; Blasco et al., 2019).

851 In addition, our results highlight that the sub-shelf melting has a very
852 strong control on the simulated grounding-line discharge. At the northern
853 ice sheet margin, the grounding-line flux curve remains nearly flat, with
854 minor oscillations due to changes in the eustatic sea level, until the sub-
855 shelf melting starts to increase after 15 ky BP (Fig. 8). In contrast, the
856 alternation of increasing/decreasing trends in sub-shelf melting at the western
857 ice sheet margin corresponds to intervals of increasing/decreasing grounding-
858 line discharge (Fig. 8). We focus in particular on the interval 17-15 ky BP,
859 which is marked by the collapse of the junction between the BSIS and the
860 SIS in the central Barents Sea. During this time interval, the eustatic sea
861 level is relatively stable (Fig. 8) and the ocean thermal forcing below 200

862 meters slowly, gradually increase from around 5 to 20 °C² (Fig. 3B), which
863 corresponds to an increase in ocean temperatures above freezing of around
864 +2.3 °C in two thousand years (around 0.1 °C per century). This prescribed
865 ocean warming causes a 35% increase in sub-shelf melting (+25 Gt/yr), which
866 results in turn in a 65% increase in grounding-line discharge (+150 Gt/yr)
867 and a nearly doubled rate of sea level rise from 0.56 to 1.04 mm/yr (Fig. 8 and
868 Table 3). This shows that a prolonged, gradual ocean warming is capable of
869 triggering sustained grounded ice discharge over multi-millennial timescales,
870 even without including positive feedbacks such as MISI, acknowledged to play
871 a role at least as important as the oceanic forcing in Antarctica (Joughin
872 et al., 2014; Rignot et al., 2014; Jenkins et al., 2018), and MICI. Recent
873 observations showed significant ocean warming over the last decades in the
874 Bellingshausen and Amundsen shelves in West Antarctica, at trends of 0.1-
875 0.3 °C per decade (Schmidtke et al., 2014). These trends of ocean warming
876 are at least one order of magnitude larger than those driving the collapse
877 of the BSIS-SIS junction in the central Barents Sea between 17 and 15 ky
878 BP. This suggests that if current trends will continue, the long-term stability
879 of the Bellingshausen and Amundsen sectors in West Antarctica could be
880 already at stake within the next centuries.

881 Finally, it is remarked that a similar south-west to north-east deglaciation
882 pattern has also recently been obtained with a first-order ice sheet model
883 (Patton et al., 2017). It is stressed that our study differs fundamentally from
884 (Patton et al., 2017) because of methodological differences in the treatment
885 of climatic and oceanic forcing as drivers of the ice sheet simulations. In
886 fact, reference climatology and associated climate forcings in (Patton et al.,

887 2017) have been regionally tuned in order to match a suite of empirical data,
 888 and the retreat of the marine-terminating ice sheet margins is regulated by
 889 an empirical function relating calving to ice thickness and water depth. In
 890 this study, we focused instead on providing a simulated scenario of the last
 891 deglaciation of the BSIS reflecting the original climatic and oceanic forcings.
 892 For this reason, a more meaningful direct comparison between the two studies
 893 is not possible.

Simulation Time	Model/DATED-1 Agreement	Model/DATED-1 Overestimation	Model/DATED-1 Underestimation
21 ky BP	2.3 Mkm ² (85%)	0.3 Mkm ² (12%)	0.1 Mkm ² (3%)
20 ky BP	2.2 Mkm ² (85%)	0.3 Mkm ² (10%)	0.1 Mkm ² (5%)
19 ky BP	2.0 Mkm ² (83%)	0.2 Mkm ² (9%)	0.2 Mkm ² (8%)
18 ky BP	1.5 Mkm ² (66%)	0.5 Mkm ² (24%)	0.2 Mkm ² (10%)
17 ky BP	1.4 Mkm ² (66%)	0.6 Mkm ² (26%)	0.2 Mkm ² (8%)
16 ky BP	1.1 Mkm ² (63%)	0.6 Mkm ² (33%)	0.1 Mkm ² (4%)
15 ky BP	0.8 Mkm ² (60%)	0.5 Mkm ² (38%)	<0.1 Mkm ² (2%)
14 ky BP	0.3 Mkm ² (60%)	0.2 Mkm ² (38%)	<0.1 Mkm ² (2%)
13 ky BP	0.3 Mkm ² (62%)	0.2 Mkm ² (34%)	<0.1 Mkm ² (4%)

Table 4: Simulated/DATED-1 ice sheet area agreement, overestimation and underestimation between the group of “admissible simulations” and the DATED-1 reconstruction throughout the deglaciation. Values are expressed both in Mkm² and as a percentage of the total ice sheet area $A_{TOT} = (A_s \cap A_D) \cup (A_s \setminus A_D) \cup (A_D \setminus A_s)$, where A_s is the simulated area and A_D is the DATED-1 area.

Barents Sea ice sheet							
Time	Ice volume	SLR rate	Ice area	Rate of area loss	Shelf area	Sub-shelf melting	
21 ky BP	8.74 m SLE	-	2.42 Mkm ²	-	0.13 Mkm ²	12 Gt/yr	
20 ky BP	7.98 m SLE	0.75 mm/yr	2.27 Mkm ²	150 km ² /yr	0.15Mkm ²	44 Gt/yr	
19 ky BP	7.10 m SLE	0.88 mm/yr	2.08 Mkm ²	180 km ² /yr	0.23 Mkm ²	77 Gt/yr	
18 ky BP	6.20 m SLE	0.90 mm/yr	1.94 Mkm ²	150 km ² /yr	0.26 Mkm ²	72 Gt/yr	
17 ky BP	5.44 m SLE	0.75 mm/yr	1.86 Mkm ²	70 km ² /yr	0.29 Mkm ²	69 Gt/yr	
16 ky BP	4.62 m SLE	0.82 mm/yr	1.69 Mkm ²	180 km ² /yr	0.37 Mkm ²	75 Gt/yr	
15 ky BP	3.36 m SLE	1.27 mm/yr	1.29 Mkm ²	390 km ² /yr	0.38 Mkm ²	100 Gt/yr	
14.4 ky BP	2.17 m SLE	1.97 mm/yr	0.88 Mkm ²	690 km ² /yr	0.45 Mkm ²	310 Gt/yr	
14 ky BP	1.40 m SLE	1.95 mm/yr	0.70 Mkm ²	450 km ² /yr	0.38 Mkm ²	171 Gt/yr	
13 ky BP	0.45 m SLE	0.94 mm/yr	0.41 Mkm ²	290 km ² /yr	0.23 Mkm ²	37 Gt/yr	
Western/Central Barents Sea							
Time	Ice volume	SLR rate	Ice area	Rate of area loss	Shelf area	Sub-shelf melting	
21 ky BP	5.57 m SLE	-	1.47 Mkm ²	-	0.04 Mkm ²	5 Gt/yr	
20 ky BP	5.09 m SLE	0.48 mm/yr	1.37 Mkm ²	110 km ² /yr	0.06 Mkm ²	44 Gt/yr	
19 ky BP	4.47 m SLE	0.61 mm/yr	1.24 Mkm ²	130 km ² /yr	0.12 Mkm ²	76 Gt/yr	
18 ky BP	3.82 m SLE	0.65 mm/yr	1.13 Mkm ²	110 km ² /yr	0.15 Mkm ²	71 Gt/yr	
17 ky BP	3.26 m SLE	0.56 mm/yr	1.07 Mkm ²	60 km ² /yr	0.19 Mkm ²	69 Gt/yr	
16 ky BP	2.64 m SLE	0.62 mm/yr	0.94 Mkm ²	140 km ² /yr	0.26 Mkm ²	74 Gt/yr	
15 ky BP	1.59 m SLE	1.04 mm/yr	0.61 Mkm ²	320 km ² /yr	0.25 Mkm ²	95 Gt/yr	
14.4 ky BP	0.80 m SLE	1.32 mm/yr	0.35 Mkm ²	450 km ² /yr	0.25 Mkm ²	294 Gt/yr	
14 ky BP	0.37 m SLE	1.07 mm/yr	0.25 Mkm ²	230 km ² /yr	0.19 Mkm ²	110 Gt/yr	
13 ky BP	0.19 m SLE	0.19 mm/yr	0.20 Mkm ²	40 km ² /yr	0.08 Mkm ²	4 Gt/yr	
Northern/Eastern Barents Sea							
Time	Ice volume	SLR rate	Ice area	Rate of area loss	Shelf area	Sub-shelf melting	
21 ky BP	3.27 m SLE	-	0.97 Mkm ²	-	0.09 Mkm ²	8 Gt/yr	
20 ky BP	2.99 m SLE	0.28 mm/yr	0.93 Mkm ²	40 km ² /yr	0.09 Mkm ²	<1 Gt/yr	
19 ky BP	2.72 m SLE	0.27 mm/yr	0.87 Mkm ²	50 km ² /yr	0.11 Mkm ²	<1 Gt/yr	
18 ky BP	2.46 m SLE	0.25 mm/yr	0.83 Mkm ²	40 km ² /yr	0.12 Mkm ²	<1 Gt/yr	
17 ky BP	2.27 m SLE	0.20 mm/yr	0.82 Mkm ²	10 km ² /yr	0.11 Mkm ²	<1 Gt/yr	
16 ky BP	2.06 m SLE	0.20 mm/yr	0.77 Mkm ²	40 km ² /yr	0.12 Mkm ²	<1 Gt/yr	
15 ky BP	1.84 m SLE	0.23 mm/yr	0.70 Mkm ²	70 km ² /yr	0.13 Mkm ²	5 Gt/yr	
14.4 ky BP	1.42 m SLE	0.69 mm/yr	0.55 Mkm ²	255 km ² /yr	0.20 Mkm ²	20 Gt/yr	
14 ky BP	1.04 m SLE	0.95 mm/yr	0.46 Mkm ²	220 km ² /yr	0.20 Mkm ²	70 Gt/yr	
13 ky BP	0.26 m SLE	0.78 mm/yr	0.21 Mkm ²	250 km ² /yr	0.16 Mkm ²	32 Gt/yr	

Table 3: Integrated ice volume, sea level rise rate, ice area, rate of ice area loss, ice shelf area and sub-shelf melting throughout the deglaciation in the average simulated scenario.

895 5. Conclusions

896 A perturbed physics ensemble of transient ice sheet model simulations
897 has been performed to investigate the evolution of the BSIS during the last
898 deglaciation. The simulations are forced with transient macro-regional atmo-
899 spheric and oceanic conditions and a transient eustatic sea level curve. The
900 ensemble of transient simulations has been validated against the DATED-1
901 reconstruction to construct average, minimum and maximum deglaciation
902 scenarios. The simulated deglaciation scenarios have been then analyzed
903 and compared with the the DATED-1 reconstruction (Hughes et al., 2016),
904 providing the following insights:

- 905 • The simulated deglaciation starts immediately after the LGM, with a
906 rapid retreat of the western ice sheet margin into the central Barents Sea
907 between 21 and 18 ky BP. This simulated retreat is primarily driven by the
908 ocean forcing prescribed at the western ice sheet margin, with the initial eu-
909 static sea level rise amplifying the ice sheet sensitivity to sub-shelf melting.
910 The initial simulated retreat of the western ice sheet margin is not sup-
911 ported by the DATED-1 reconstruction, suggesting that the western margin
912 remained stable until 19 ky BP. This mismatch can be explained either by
913 an excessive model sensitivity to sub-shelf melting, or by an overestimation
914 of the subsurface Atlantic water temperature in the TraCE21ka simulation,
915 likely amplified by the relatively simple sub-shelf melting parametrisation
916 used in this study.

- 917 • The simulated eastern ice sheet margin remains extremely stable until
918 15 ky BP, due to the cold atmospheric and oceanic conditions prescribed over

919 this area. This is in clear contradiction with the DATED-1 reconstruction,
920 suggesting a very rapid retreat of this margin between 19 and 18 ky BP. A
921 first consideration to explain the model/data mismatch is that our simula-
922 tions do not account for variations in relative sea level, which might have
923 triggered the initial eastern margin retreat in spite of the cold climatic con-
924 ditions. However, we also note that the eastern margin position throughout
925 the deglaciation is highly uncertain in the DATED-1 reconstruction (Hughes
926 et al., 2016). It cannot be therefore excluded that the model-data mismatch
927 observed in this region might be overestimated and the eastern margin ex-
928 perience a slower, steady retreat during this time interval.

929 • The disintegration of the connection between the SIS and the BSIS in
930 the central Barents Sea occurs between 16 and 15 ky BP in the simulated
931 average and maximum scenarios, whereas the minimum simulated scenario
932 suggests instead that this event occurred earlier between 17 and 16 ky BP.
933 The simulated scenarios are in good agreement with the DATED-1 scenarios
934 for the timing of this event, placed between 16 and 15 ky BP in the most-
935 credible and minimum reconstructions and between 17 and 16 ky BP in the
936 maximum reconstruction. The collapse of the BSIS-SIS junction is driven by
937 a slow, gradual increase in the prescribed Barents Sea ocean forcing below
938 200 meters depth after 17 ky BP.

939 • The final simulated ice sheet collapse takes place between 15 and 13 ky
940 BP, driven by the increase in the prescribed ocean forcing both in the Barents
941 Sea and in the Arctic Ocean. The abrupt eustatic sea level rise prescribed
942 between 14.6 and 14.4 ky BP contribute to accelerate the ice sheet collapse
943 in the central Barents Sea and, to a less extent, in the northern Barents Sea.

944 The simulated scenarios are in agreement with the DATED-1 reconstruction
945 on the timing of the final ice sheet final collapse, with the exception of few
946 ice remnants in the Kara Sea.

947 • Overall, the simulated deglacial evolution of the BSIS exhibits a clear
948 south-west to north-east deglaciation pattern, primarily driven by the ocean
949 forcing at the western and northern ice sheet margins. Prescribed eustatic sea
950 level rise contributes to amplify the ice sheet sensitivity to sub-shelf melting
951 over relatively short time intervals. The strong impact of sub-shelf melting
952 on the retreat of marine-based ice sheets has also been recently demonstrated
953 in ice sheet modelling studies focusing on the multi-millennial evolution of
954 the Eurasian ice sheets (Alvarez-Solas et al., 2019) and the Antarctic Ice
955 Sheet (Mackintosh et al., 2011; Lowry et al., 2019; Blasco et al., 2019).

956 • Our results highlight that the sub-shelf melting has a very strong con-
957 trol on the simulated grounding-line discharge. In particular, the collapse of
958 the junction between the BSIS and the SIS in the central Barents Sea occurs
959 in response to an increase in ocean temperatures above freezing of around
960 $+2.3^{\circ}\text{C}$ in two thousand years (around 0.1°C per century). This prescribed
961 ocean warming results in a 65% increase in grounding-line discharge and a
962 nearly doubled rate of sea level rise, thus showing that a prolonged, gradual
963 ocean warming is capable of triggering sustained grounded ice discharge over
964 multi-millennial timescales, even without including positive feedbacks such
965 as MISI and MICI.

966 **Acknowledgements**

967 The research reported in this work was supported by Oceanography and
968 Applied Geophysics (OGS) and CINECA under HPC-TRES program award
969 number 2016-03 and by the FORMAS grant 214-2013-1600 to NK. We ac-
970 knowledge the CINECA award under the ISCRA initiative, for the avail-
971 ability of high performance computing resources and support. Parts of the
972 computations were performed on resources provided by the Swedish National
973 Infrastructure for Computing (SNIC) at PDC Center for High Performance
974 Computing at KTH. MP was supported by a Bjerknes Visiting Fellowship
975 from the Bjerknes Centre for Climate Research in July 2018. JM and ALCH
976 acknowledge the strategic project RISES funded by the Bjerknes Centre for
977 Climate Research, Norway. The authors would like to thank the anonymous
978 reviewers for their valuable comments and suggestions to improve the quality
979 of the paper.

- 980 Abe-Ouchi, A., Segawa, T., Saito, F.. Climatic conditions for modelling
981 the Northern Hemisphere ice sheets throughout the ice age cycle. *Climate*
982 *of the Past* 2007;3(3):423–438.
- 983 Alvarez-Solas, J., Banderas, R., Robinson, A., Montoya, M.. Ocean-driven
984 millennial-scale variability of the Eurasian ice sheet during the last glacial
985 period simulated with a hybrid ice-sheet–shelf model. *Climate of the Past*
986 2019;15(3):957–979.
- 987 Álvarez Solás, J., Montoya, M., Ritz, C., Ramstein, G., Charbit, S.,
988 Dumas, C., Nisancioglu, K., Dokken, T., Ganopolski, A.. Heinrich
989 event 1: an example of dynamical ice-sheet reaction to oceanic changes.
990 *Climate of the Past* 2011;7(4):1297–1306.
- 991 Andersen, E.S., Dokken, T.M., Elverhøi, A., Solheim, A., Fossen, I..
992 Late Quaternary sedimentation and glacial history of the western Svalbard
993 continental margin. *Marine Geology* 1996;133(3-4):123–156.
- 994 Andersen, K.K., Azuma, N., Barnola, J., Bigler, M., et al. High-resolution
995 record of Northern Hemisphere climate extending into the last interglacial
996 period. *Nature* 2004;431(7005):147.
- 997 Andreassen, K., Winsborrow, M.. Signature of ice streaming in
998 Bjørnøyrenna, Polar North Atlantic, through the Pleistocene and impli-
999 cations for ice-stream dynamics. *Annals of Glaciology* 2009;50(52):17–26.
- 1000 Applegate, P.J., Parizek, B.R., Nicholas, R.E., Alley, R.B., Keller, K..
1001 Increasing temperature forcing reduces the Greenland Ice Sheets response
1002 time scale. *Climate dynamics* 2015;45(7-8):2001–2011.

- 1003 Barthel, A., Agosta, C., Little, C.M., Hattermann, T., Jourdain, N.C.,
1004 Goelzer, H., Nowicki, S., Seroussi, H., Straneo, F., Bracegirdle, T.J.,
1005 CMIP5 model selection for ISMIP6 ice sheet model forcing: Greenland
1006 and Antarctica; 2019. Under review for the journal *The Cryosphere* (CT).
- 1007 Bartlein, P.J., Harrison, S., Brewer, S., Connor, S., Davis, B., Gajewski,
1008 K., Guiot, J., Harrison-Prentice, T., Henderson, A., Peyron, O., et al.
1009 Pollen-based continental climate reconstructions at 6 and 21 ka: a global
1010 synthesis. *Climate Dynamics* 2011;37(3-4):775–802.
- 1011 Bjarnadóttir, L.R., Winsborrow, M.C., Andreassen, K.. Deglaciation of
1012 the central Barents Sea. *Quaternary Science Reviews* 2014;92:208–226.
- 1013 Blasco, J., Tabone, I., Alvarez-Solas, J., Robinson, A., Montoya, M.. The
1014 Antarctic Ice Sheet response to glacial millennial-scale variability. *Climate*
1015 *of the Past* 2019;15(1):121–133.
- 1016 Braconnot, P., Harrison, S.P., Kageyama, M., Bartlein, P.J., Masson-
1017 Delmotte, V., Abe-Ouchi, A., Otto-Bliesner, B., Zhao, Y.. Evalua-
1018 tion of climate models using palaeoclimatic data. *Nature Climate Change*
1019 2012;2(6):417–424.
- 1020 Braithwaite, R.J.. Calculation of degree-days for glacier-climate research.
1021 *Zeitschrift für Gletscherkunde und Glazialgeologie* 1984;20:1–8.
- 1022 Charbit, S., Ritz, C., Ramstein, G.. Simulations of Northern Hemisphere
1023 ice-sheet retreat: sensitivity to physical mechanisms involved during the
1024 Last Deglaciation. *Quaternary Science Reviews* 2002;21(1-3):243–265.

- 1025 Chauhan, T., Rasmussen, T., Noormets, R., Jakobsson, M., Hogan,
1026 K.. Glacial history and paleoceanography of the southern Yermak Plateau
1027 since 132 ka BP. *Quaternary Science Reviews* 2014;92:155–169.
- 1028 Chauhan, T., Rasmussen, T.L., Noormets, R.. Palaeoceanography of the
1029 Barents Sea continental margin, north of Nordaustlandet, Svalbard, during
1030 the last 74 ka. *Boreas* 2016;45(1):76–99.
- 1031 Cofaigh, C.Ó., Weilbach, K., Lloyd, J.M., Benetti, S., Callard, S.L.,
1032 Purcell, C., Chiverrell, R.C., Dunlop, P., Saher, M., Livingstone, S.J.,
1033 et al. Early deglaciation of the British-Irish Ice Sheet on the Atlantic shelf
1034 northwest of Ireland driven by glacioisostatic depression and high relative
1035 sea level. *Quaternary Science Reviews* 2019;208:76–96.
- 1036 Colleoni, F., De Santis, L., Siddoway, C.S., Bergamasco, A., Golledge,
1037 N.R., Lohmann, G., Passchier, S., Siegert, M.J.. Publisher Correction:
1038 Spatio-temporal variability of processes across Antarctic ice-bed–ocean in-
1039 terfaces. *Nature communications* 2018;9(1):2742.
- 1040 Colleoni, F., Quiquet, A., Masina, S.. Long-term safety of a planned
1041 geological repository for spent nuclear fuel in Forsmark – Phase 2: Impact
1042 of ice sheet dynamics, climat forcing and multi-variate sensitivity analysis
1043 on maximum ice sheet thickness. Technical Report SKB TR-14-21; Swedish
1044 Nuclear Fuel and Waste Management Co, Stockholm, Sweden; 2016.
- 1045 Cook, A., Holland, P., Meredith, M., Murray, T., Luckman, A., Vaughan,
1046 D.. Ocean forcing of glacier retreat in the western Antarctic Peninsula.
1047 *Science* 2016;353(6296):283–286.

- 1048 De Vernal, A., Eynaud, F., Henry, M., Hillaire-Marcel, C., Londeix, L.,
1049 Mangin, S., Matthießen, J., Marret, F., Radi, T., Rochon, A., et al.
1050 Reconstruction of sea-surface conditions at middle to high latitudes of the
1051 Northern Hemisphere during the Last Glacial Maximum (LGM) based on
1052 dinoflagellate cyst assemblages. *Quaternary Science Reviews* 2005;24(7-
1053 9):897–924.
- 1054 DeConto, R.M., Pollard, D.. Contribution of Antarctica to past and future
1055 sea-level rise. *Nature* 2016;531(7596):591.
- 1056 Dowdeswell, J.A., Hogan, K., Evans, J., Noormets, R., Ó Cofaigh, C.,
1057 Ottesen, D.. Past ice-sheet flow east of Svalbard inferred from streamlined
1058 subglacial landforms. *Geology* 2010;38(2):163–166.
- 1059 Dowdeswell, J.A., Siegert, M.J.. Ice-sheet numerical modeling and ma-
1060 rine geophysical measurements of glacier-derived sedimentation on the
1061 Eurasian Arctic continental margins. *Geological Society of America Bul-
1062 letin* 1999;111(7):1080–1097.
- 1063 Dumas, C.. Modélisation de l'évolution de l'Antarctique depuis le dernier cy-
1064 cle glaciaire-interglaciaire jusqu'au futur: importance relative des différents
1065 processus physiques et rôle des données d'entrée. Ph.D. thesis; Université
1066 Joseph-Fourier-Grenoble I; 2002.
- 1067 Edwards, T.L., Brandon, M.A., Durand, G., Edwards, N.R., Golledge,
1068 N.R., Holden, P.B., Nias, I.J., Payne, A.J., Ritz, C., Wernecke, A..
1069 Revisiting Antarctic ice loss due to marine ice-cliff instability. *Nature*
1070 2019;566(7742):58.

- 1071 Esteves, M., Bjarnadóttir, L.R., Winsborrow, M.C., Shackleton, C.S.,
1072 Andreassen, K.. Retreat patterns and dynamics of the Sentral-
1073 bankrenna glacial system, central Barents Sea. *Quaternary Science Re-*
1074 *views* 2017;169:131–147.
- 1075 Fausto, R.S., Ahlstrøm, A.P., Van As, D., Bøggild, C.E., Johnsen, S.J..
1076 A new present-day temperature parameterization for Greenland. *Journal*
1077 *of Glaciology* 2009;55(189):95–105.
- 1078 Fausto, R.S., Ahlstrøm, A.P., Van As, D., Steffen, K.. Present-day
1079 temperature standard deviation parameterization for Greenland. *Journal*
1080 *of Glaciology* 2011;57(206):1181–1183.
- 1081 Favier, L., Durand, G., Cornford, S.L., Gudmundsson, G.H., Gagliardini,
1082 O., Gillet-Chaulet, F., Zwinger, T., Payne, A., Le Brocq, A.M.. Retreat
1083 of Pine Island Glacier controlled by marine ice-sheet instability. *Nature*
1084 *Climate Change* 2014;4(2):117.
- 1085 Favier, L., Jourdain, N.C., Jenkins, A., Merino, N., Durand,
1086 G., Gagliardini, O., Gillet-Chaulet, F., Mathiot, P.. As-
1087 sessment of Sub-Shelf Melting Parameterisations Using the Ocean-
1088 Ice Sheet Coupled Model NEMO(v3.6)-Elmer/Ice(v8.3). *Geo-*
1089 *scientific Model Development Discussions* 2019;2019:1–40. URL:
1090 <https://www.geosci-model-dev-discuss.net/gmd-2019-26/>.
1091 doi:10.5194/gmd-2019-26.
- 1092 Fransner, O., Noormets, R., Chauhan, T., ORegan, M., Jakobsson,

- 1093 M.. Late Weichselian ice stream configuration and dynamics in Albertini
1094 Trough, northern Svalbard margin. *arktos* 2018;4(1):1.
- 1095 Fransner, O., Noormets, R., Flink, A., Hogan, K., O'Regan, M., Jakobs-
1096 son, M.. Glacial landforms and their implications for glacier dynamics in
1097 Rijpfjorden and Duvefjorden, northern Nordaustlandet, Svalbard. *Journal*
1098 *of Quaternary Science* 2017;32(3):437–455.
- 1099 Goelzer, H., Huybrechts, P., Loutre, M.F., Gooose, H., Fichefet, T.,
1100 Mouchet, A.. Impact of Greenland and Antarctic ice sheet interactions
1101 on climate sensitivity. *Climate Dynamics* 2011;37(5-6):1005–1018.
- 1102 Gregoire, L.J., Otto-Bliesner, B., Valdes, P.J., Ivanovic, R.. Abrupt Bølling
1103 warming and ice saddle collapse contributions to the Meltwater Pulse 1a
1104 rapid sea level rise. *Geophysical research letters* 2016;43(17):9130–9137.
- 1105 Greve, R.. Relation of measured basal temperatures and the spatial distri-
1106 bution of the geothermal heat flux for the Greenland ice sheet. *Annals of*
1107 *Glaciology* 2005;42:424–432.
- 1108 Greve, R., Saito, F., Abe-Ouchi, A.. Initial results of the SeaRISE numeri-
1109 cal experiments with the models SICOPOLIS and IcIES for the Greenland
1110 ice sheet. *Annals of Glaciology* 2011;52(58):23–30.
- 1111 Gudmundsson, H., Krug, J., Durand, G., Favier, L., Gagliardini, O..
1112 The stability of grounding lines on retrograde slopes. *The Cryosphere*
1113 2012;6(6):1497–1505.
- 1114 Hogan, K., Dowdeswell, J., Noormets, R., Evans, J., Cofaigh, C.Ó., Jakob-
1115 sson, M.. Submarine landforms and ice-sheet flow in the Kvitøya Trough,

- 1116 northwestern Barents Sea. *Quaternary Science Reviews* 2010a;29(25-
1117 26):3545–3562.
- 1118 Hogan, K.A., Dowdeswell, J.A., Noormets, R., Evans, J., Cofaigh, C.Ó..
1119 Evidence for full-glacial flow and retreat of the Late Weichselian Ice Sheet
1120 from the waters around Kong Karls Land, eastern Svalbard. *Quaternary*
1121 *Science Reviews* 2010b;29(25-26):3563–3582.
- 1122 Holland, P.R., Jenkins, A., Holland, D.M.. The response of ice shelf
1123 basal melting to variations in ocean temperature. *Journal of Climate*
1124 2008;21(11):2558–2572.
- 1125 Hughes, A.L., Gyllencreutz, R., Lohne, Ø.S., Mangerud, J., Svendsen,
1126 J.I.. The last Eurasian ice sheets—a chronological database and time-slice
1127 reconstruction, DATED-1. *Boreas* 2016;45(1):1–45.
- 1128 Hütter, K.. *Theoretical Glaciology: Material Science of Ice and the Me-*
1129 *chanics of Glacier and Ice Sheets*, 510 pp. D Reidel, Norwell, Mass 1983;.
- 1130 Ivanovic, R., Gregoire, L., Burke, A., Wickert, A., Valdes, P., Ng, H.,
1131 Robinson, L., McManus, J., Mitrovica, J., Lee, L., et al. Acceleration
1132 of northern ice sheet melt induces AMOC slowdown and northern cool-
1133 ing in simulations of the early last deglaciation. *Paleoceanography and*
1134 *Paleoclimatology* 2018;33(7):807–824.
- 1135 Jakobsson, M.. *International bathymetric chart of the Arctic Ocean (IB-*
1136 *CAO)*. Springer, 2014.
- 1137 Jenkins, A., Shoosmith, D., Dutrieux, P., Jacobs, S., Kim, T.W., Lee,
1138 S.H., Ha, H.K., Stammerjohn, S.. West Antarctic Ice Sheet retreat in the

- 1139 Amundsen Sea driven by decadal oceanic variability. *Nature Geoscience*
1140 2018;11(10):733–738.
- 1141 Joughin, I., Smith, B.E., Medley, B.. Marine ice sheet collapse poten-
1142 tially under way for the Thwaites Glacier Basin, West Antarctica. *Science*
1143 2014;344(6185):735–738.
- 1144 Khazendar, A., Rignot, E., Schroeder, D.M., Seroussi, H., Schodlok, M.P.,
1145 Scheuchl, B., Mouginot, J., Sutterley, T.C., Velicogna, I.. Rapid subma-
1146 rine ice melting in the grounding zones of ice shelves in West Antarctica.
1147 *Nature communications* 2016;7:13243.
- 1148 Kirchner, N., Hutter, K., Jakobsson, M., Gyllencreutz, R.. Capabilities and
1149 limitations of numerical ice sheet models: a discussion for Earth-scientists
1150 and modelers. *Quaternary Science Reviews* 2011;30(25-26):3691–3704.
- 1151 Kleiber, H., Knies, J., Niessen, F.. The Late Weichselian glaciation of the
1152 Franz Victoria Trough, northern Barents Sea: ice sheet extent and timing.
1153 *Marine Geology* 2000;168(1-4):25–44.
- 1154 Landvik, J.Y., Bondevik, S., Elverhøi, A., Fjeldskaar, W., Mangerud, J.,
1155 Salvigsen, O., Siegert, M.J., Svendsen, J.I., Vorren, T.O.. The last
1156 glacial maximum of Svalbard and the Barents Sea area: ice sheet extent
1157 and configuration. *Quaternary Science Reviews* 1998;17(1):43–75.
- 1158 Laske, G.. A global digital map of sediment thickness. *Eos Trans AGU*
1159 1997;78:F483.
- 1160 Lazeroms, W.M., Jenkins, A., Gudmundsson, G.H., Van De Wal,
1161 R.S.. Modelling present-day basal melt rates for Antarctic ice shelves

1162 using a parametrization of buoyant meltwater plumes. *The Cryosphere*
1163 2018;12(1):49–70.

1164 Le Meur, E., Huybrechts, P.. A comparison of different ways of dealing
1165 with isostasy: examples from modelling the Antarctic ice sheet during the
1166 last glacial cycle. *Annals of Glaciology* 1996;23:309–317.

1167 Liu, Z., Otto-Bliesner, B., He, F., Brady, E., Tomas, R., Clark, P.,
1168 Carlson, A., Lynch-Stieglitz, J., Curry, W., Brook, E., et al. Transient
1169 simulation of last deglaciation with a new mechanism for Bølling-Allerød
1170 warming. *Science* 2009;325(5938):310–314.

1171 Llopart, J., Urgeles, R., Camerlenghi, A., Lucchi, R.G., Rebesco, M.,
1172 De Mol, B.. Late quaternary development of the Storfjorden and Kveithola
1173 trough mouth fans, northwestern Barents Sea. *Quaternary Science Reviews*
1174 2015;129:68–84.

1175 Lowry, D.P., Golledge, N.R., Bertler, N.A., Jones, R.S., McKay,
1176 R.. Deglacial grounding-line retreat in the Ross Embayment, Antarc-
1177 tica, controlled by ocean and atmosphere forcing. *Science advances*
1178 2019;5(8):eaav8754.

1179 Lucchi, R., Camerlenghi, A., Rebesco, M., Colmenero-Hidalgo, E., Sierro,
1180 F., Sagnotti, L., Urgeles, R., Melis, R., Morigi, C., Bárcena, M.A.,
1181 et al. Postglacial sedimentary processes on the Storfjorden and Kveithola
1182 trough mouth fans: Significance of extreme glacimarine sedimentation.
1183 *Global and planetary change* 2013;111:309–326.

- 1184 Ma, Y., Gagliardini, O., Ritz, C., Gillet-Chaulet, F.,
1185 Durand, G., Montagnat, M.. Enhancement factors for
1186 grounded ice and ice shelves inferred from an anisotropic ice-
1187 flow model. *Journal of Glaciology* 2010;56(199):805–812(8).
1188 URL: <https://hal-insu.archives-ouvertes.fr/insu-00653459>.
1189 doi:10.3189/002214310794457209.
- 1190 MacAyeal, D.R.. Large-scale ice flow over a viscous basal sediment: The-
1191 ory and application to ice stream B, Antarctica. *Journal of Geophysical*
1192 *Research: Solid Earth* 1989;94(B4):4071–4087.
- 1193 Mackintosh, A., Golledge, N., Domack, E., Dunbar, R., Leventer, A.,
1194 White, D., Pollard, D., DeConto, R., Fink, D., Zwartz, D., et al.
1195 Retreat of the East Antarctic ice sheet during the last glacial termination.
1196 *Nature Geoscience* 2011;4(3):195.
- 1197 Marshall, S.J., Sharp, M.J., Burgess, D.O., Anslow, F.S.. Near-surface-
1198 temperature lapse rates on the Prince of Wales Icefield, Ellesmere Island,
1199 Canada: Implications for regional downscaling of temperature. *International*
1200 *Journal of Climatology: A Journal of the Royal Meteorological So-*
1201 *ciety* 2007;27(3):385–398.
- 1202 Marsiat, I.. Simulation of the Northern Hemisphere continental ice
1203 sheets over the last glacial-interglacial cycle: experiments with a latitude-
1204 longitude vertically integrated ice sheet model coupled to a zonally aver-
1205 aged climate model. *Paleoclimates* 1994;1(1):59–98.
- 1206 Martin, M., Winkelmann, R., Haseloff, M., Albrecht, T., Bueler, E.,

- 1207 Khroulev, C., Levermann, A.. The Potsdam Parallel Ice Sheet Model
1208 (PISM-PIK)–Part 2: Dynamic equilibrium simulation of the Antarctic ice
1209 sheet. *The Cryosphere* 2011;5(3):727–740.
- 1210 McManus, J.F., Francois, R., Gherardi, J.M., Keigwin, L.D., Brown-Leger,
1211 S.. Collapse and rapid resumption of Atlantic meridional circulation linked
1212 to deglacial climate changes. *Nature* 2004;428(6985):834.
- 1213 Mercer, J.H.. A former ice sheet in the Arctic Ocean? *Palaeogeography,*
1214 *Palaeoclimatology, Palaeoecology* 1970;8(1):19–27.
- 1215 Morland, L.. Thermomechanical balances of ice sheet flows. *Geophysical &*
1216 *Astrophysical Fluid Dynamics* 1984;29(1-4):237–266.
- 1217 Newton, A., Knutz, P., Huuse, M., Gannon, P., Brocklehurst, S., Clausen,
1218 O., Gong, Y.. Ice stream reorganization and glacial retreat on the north-
1219 west Greenland shelf. *Geophysical Research Letters* 2017;44(15):7826–
1220 7835.
- 1221 Ng, H.C., Robinson, L.F., McManus, J.F., Mohamed, K.J., Jacobel,
1222 A.W., Ivanovic, R.F., Gregoire, L.J., Chen, T.. Coherent deglacial
1223 changes in western Atlantic Ocean circulation. *Nature communications*
1224 2018;9(1):1–10.
- 1225 Nielsen, T., Rasmussen, T.L.. Reconstruction of ice sheet retreat after the
1226 Last Glacial maximum in Storfjorden, southern Svalbard. *Marine Geology*
1227 2018;402:228–243.
- 1228 Nørgaard-Pedersen, N., Spielhagen, R.F., Erlenkeuser, H., Grootes, P.M.,
1229 Heinemeier, J., Knies, J.. Arctic Ocean during the Last Glacial Maximum:

- 1230 Atlantic and polar domains of surface water mass distribution and ice
1231 cover. *Paleoceanography* 2003;18(3).
- 1232 Ottesen, D., Dowdeswell, J., Rise, L.. Submarine landforms and the
1233 reconstruction of fast-flowing ice streams within a large Quaternary ice
1234 sheet: the 2500-km-long Norwegian-Svalbard margin (57–80 N). *Geological*
1235 *Society of America Bulletin* 2005;117(7-8):1033–1050.
- 1236 Paolo, F.S., Fricker, H.A., Padman, L.. Volume loss from Antarctic ice
1237 shelves is accelerating. *Science* 2015;348(6232):327–331.
- 1238 Patton, H., Andreassen, K., Bjarnadóttir, L.R., Dowdeswell, J.A., Wins-
1239 borrow, M.C., Noormets, R., Polyak, L., Auriac, A., Hubbard, A..
1240 Geophysical constraints on the dynamics and retreat of the Barents Sea
1241 ice sheet as a paleobenchmark for models of marine ice sheet deglaciation.
1242 *Reviews of Geophysics* 2015;53(4):1051–1098.
- 1243 Patton, H., Hubbard, A., Andreassen, K., Auriac, A., Whitehouse, P.L.,
1244 Stroeven, A.P., Shackleton, C., Winsborrow, M., Heyman, J., Hall,
1245 A.M.. Deglaciation of the Eurasian ice sheet complex. *Quaternary Science*
1246 *Reviews* 2017;169:148–172.
- 1247 Patton, H., Hubbard, A., Andreassen, K., Winsborrow, M., Stroeven,
1248 A.P.. The build-up, configuration, and dynamical sensitivity of the
1249 Eurasian ice-sheet complex to Late Weichselian climatic and oceanic forc-
1250 ing. *Quaternary Science Reviews* 2016;153:97–121.
- 1251 Pedrosa, M., Camerlenghi, A., De Mol, B., Urgeles, R., Rebesco, M.,
1252 Lucchi, R.G., et al. Seabed morphology and shallow sedimentary structure

1253 of the Storfjorden and Kveithola trough-mouth fans (North West Barents
1254 Sea). *Marine Geology* 2011;286(1-4):65–81.

1255 Pelle, T., Bondzio, J.H., et al. Brief communication: PICOP, a new ocean
1256 melt parameterization under ice shelves combining PICO and a plume
1257 model. *The Cryosphere* 2019;13(3):1043–1049.

1258 Peltier, W.. Global glacial isostasy and the surface of the ice-age Earth:
1259 the ICE-5G (VM2) model and GRACE. *Annu Rev Earth Planet Sci*
1260 2004;32:111–149.

1261 Peltier, W., Argus, D., Drummond, R.. Space geodesy constrains ice age
1262 terminal deglaciation: The global ICE-6G_C (VM5a) model. *Journal of*
1263 *Geophysical Research: Solid Earth* 2015;120(1):450–487.

1264 Petrini, M.. Reconstructing with numerical Ice Sheet Models the post-
1265 LGM decay of the Eurasian Ice Sheets: data-model comparison and focus
1266 on the Storfjorden (Svalbard) ice stream dynamics history. Ph.D. thesis;
1267 Università degli Studi di Trieste; 2017.

1268 Petrini, M., Colleoni, F., Kirchner, N., Hughes, A.L., Camerlenghi, A.,
1269 Rebesco, M., Lucchi, R.G., Forte, E., Colucci, R.R., Noormets, R..
1270 Interplay of grounding-line dynamics and sub-shelf melting during retreat
1271 of the Bjørnøyrenna Ice Stream. *Scientific reports* 2018;8(1):7196.

1272 Peyaud, V., Ritz, C., Krinner, G.. Modelling the Early We-
1273 ichselian Eurasian Ice Sheets: role of ice shelves and influence of
1274 ice-dammed lakes. *Climate of the Past* 2007;3(3):375–386. URL:
1275 <https://www.clim-past.net/3/375/2007/>. doi:10.5194/cp-3-375-2007.

- 1276 Pflaumann, U., Sarnthein, M., Chapman, M., d'Abreu, L., Funnell, B.,
1277 Huels, M., Kiefer, T., Maslin, M., Schulz, H., Swallow, J., et al. Glacial
1278 North Atlantic: Sea-surface conditions reconstructed by GLAMAP 2000.
1279 *Paleoceanography* 2003;18(3).
- 1280 Piasecka, E.D., Winsborrow, M.C., Andreassen, K., Stokes, C.R.. Re-
1281 constructing the retreat dynamics of the Bjørnøyrenna Ice Stream based
1282 on new 3D seismic data from the central Barents Sea. *Quaternary Science*
1283 *Reviews* 2016;151:212–227.
- 1284 Pollard, D., DeConto, R.. Description of a hybrid ice sheet-shelf
1285 model, and application to Antarctica. *Geoscientific Model Development*
1286 2012;5(5):1273.
- 1287 Pollard, D., DeConto, R.M., Alley, R.B.. Potential Antarctic Ice Sheet
1288 retreat driven by hydrofracturing and ice cliff failure. *Earth and Planetary*
1289 *Science Letters* 2015;412:112–121.
- 1290 Polyak, L., Forman, S.L., Herlihy, F.A., Ivanov, G., Krinitsky, P..
1291 Late Weichselian deglacial history of the Svyataya (Saint) Anna Trough,
1292 northern Kara Sea, Arctic Russia. *Marine Geology* 1997;143(1-4):169–188.
- 1293 Pritchard, H., Ligtenberg, S., Fricker, H., Vaughan, D., Van den Broeke,
1294 M., Padman, L.. Antarctic ice-sheet loss driven by basal melting of ice
1295 shelves. *Nature* 2012;484(7395):502–505.
- 1296 Pritchard, M.S., Bush, A.B., Marshall, S.J.. Neglecting ice-atmosphere
1297 interactions underestimates ice sheet melt in millennial-scale deglaciation
1298 simulations. *Geophysical Research Letters* 2008;35(1).

1299 Rebesco, M., Domack, E., Zgur, F., Lavoie, C., Leventer, A., Brach-
1300 feld, S., Willmott, V., Halverson, G., Truffer, M., Scambos, T., et al.
1301 Boundary condition of grounding lines prior to collapse, Larsen-B Ice Shelf,
1302 Antarctica. *Science* 2014a;345(6202):1354–1358.

1303 Rebesco, M., Laberg, J., Pedrosa, M., Camerlenghi, A., Lucchi, R., Zgur,
1304 F., Wardell, N.. Onset and growth of trough-mouth fans on the north-
1305 western Barents Sea margin—implications for the evolution of the Barents
1306 Sea/Svalbard ice sheet. *Quaternary Science Reviews* 2014b;92:227–234.

1307 Reeh, N.. Parameterization of melt rate and surface temperature in the
1308 Greenland ice sheet. *Polarforschung* 1991;59(3):113–128.

1309 Reese, R., Albrecht, T., Mengel, M., Asay-Davis, X., Winkelmann, R..
1310 Antarctic sub-shelf melt rates via PICO. *The Cryosphere* 2018;.

1311 Rignot, E., Jacobs, S., Mouginot, J., Scheuchl, B.. Ice-shelf melting
1312 around Antarctica. *Science* 2013;341(6143):266–270.

1313 Rignot, E., Mouginot, J., Morlighem, M., Seroussi, H., Scheuchl, B..
1314 Widespread, rapid grounding line retreat of Pine Island, Thwaites, Smith,
1315 and Kohler glaciers, West Antarctica, from 1992 to 2011. *Geophysical*
1316 *Research Letters* 2014;41(10):3502–3509.

1317 Ritz, C., Rommelaere, V., Dumas, C.. Modeling the evolution of Antarctic
1318 ice sheet over the last 420,000 years: Implications for altitude changes
1319 in the Vostok region. *Journal of Geophysical Research: Atmospheres*
1320 2001;106(D23):31943–31964.

- 1321 Sarnthein, M., Pflaumann, U., Weinelt, M.. Past extent of sea ice in
1322 the northern North Atlantic inferred from foraminiferal paleotemperature
1323 estimates. *Paleoceanography* 2003;18(2).
- 1324 Schmidtko, S., Heywood, K.J., Thompson, A.F., Aoki, S.. Multidecadal
1325 warming of Antarctic waters. *Science* 2014;346(6214):1227–1231.
- 1326 Schoof, C.. Marine ice sheet stability. *Journal of Fluid Mechanics*
1327 2012;698:62–72.
- 1328 Sergienko, O., Macayeal, D.R.. Surface melting on Larsen ice shelf, Antarc-
1329 tica. *Annals of Glaciology* 2005;40:215–218.
- 1330 Seroussi, H., Nowicki, S., Simon, E., Abe-Ouchi, A., Albrecht, T.,
1331 Brondex, J., Cornford, S., Dumas, C., Gillet-Chaulet, F., Goelzer, H.,
1332 et al. initMIP-Antarctica: an ice sheet model initialization experiment of
1333 ISMIP6. *The Cryosphere* 2019;13(5):1441–1471.
- 1334 Shackleton, C.S., Winsborrow, M.C., Andreassen, K., Lucchi, R.G., Bjar-
1335 nadóttir, L.R.. Ice-margin retreat and grounding-zone dynamics during
1336 initial deglaciation of the Storfjordrenna Ice Stream, western Barents Sea.
1337 *Boreas* 2019;.
- 1338 Shapiro, N.M., Ritzwoller, M.H.. Inferring surface heat flux distributions
1339 guided by a global seismic model: particular application to Antarctica.
1340 *Earth and Planetary Science Letters* 2004;223(1-2):213–224.
- 1341 Stokes, C.R., Clark, C.D.. Palaeo-ice streams. *Quaternary Science Reviews*
1342 2001;20(13):1437–1457.

- 1343 Stokes, C.R., Tarasov, L.. Ice streaming in the Laurentide Ice Sheet:
1344 A first comparison between data-calibrated numerical model output and
1345 geological evidence. *Geophysical Research Letters* 2010;37(1).
- 1346 Stone, E., Lunt, D., Rutt, I., Hanna, E.. Investigating the sensitivity of
1347 numerical model simulations of the modern state of the Greenland ice-sheet
1348 and its future response to climate change. *The Cryosphere* 2010;4(3):397.
- 1349 Sundal, A.V., Shepherd, A., Nienow, P., Hanna, E., Palmer, S., Huy-
1350 brechts, P.. Melt-induced speed-up of Greenland ice sheet offset by efficient
1351 subglacial drainage. *Nature* 2011;469(7331):521.
- 1352 Svendsen, J.I., Alexanderson, H., Astakhov, V.I., Demidov, I., Dowdeswell,
1353 J.A., Funder, S., Gataullin, V., Henriksen, M., Hjort, C., Houmark-
1354 Nielsen, M., et al. Late Quaternary ice sheet history of northern Eurasia.
1355 *Quaternary Science Reviews* 2004;23(11-13):1229–1271.
- 1356 Tarasov, L., Dyke, A.S., Neal, R.M., Peltier, W.R.. A data-calibrated dis-
1357 tribution of deglacial chronologies for the North American ice complex from
1358 glaciological modeling. *Earth and Planetary Science Letters* 2012;315:30–
1359 40.
- 1360 Tarasov, L., Richard Peltier, W.. Greenland glacial history and local geody-
1361 namic consequences. *Geophysical Journal International* 2002;150(1):198–
1362 229.
- 1363 Tarasov, L., et al. Eurasian ice sheet evolution; –. In prep.
- 1364 Vorren, T.O., Hald, M., Lebesbye, E.. Late cenozoic environments in the
1365 Barents Sea. *Paleoceanography and Paleoclimatology* 1988;3(5):601–612.

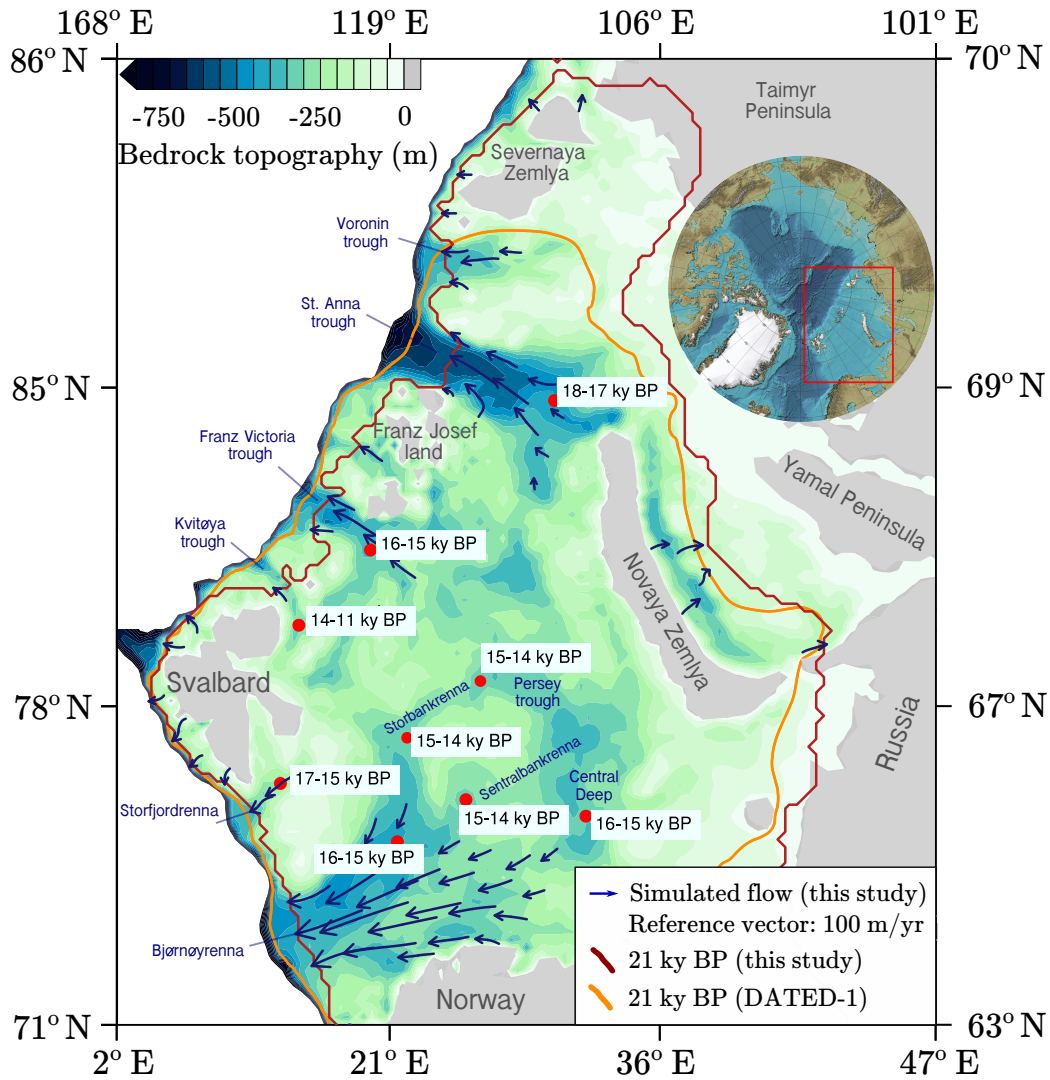


Figure 1: Bathymetric map of the Barents and Kara seas, based on the International bathymetric chart of the Arctic Ocean (IBCAO) (Jakobsson, 2014) and interpolated in the 20 km horizontal resolution ice sheet model grid. The DATED-1 (Hughes et al., 2016) (dark yellow line) and simulated (this study, dark red line) BSIS extent during the LGM are shown. Blue arrows indicate the simulated (this study) ice velocities during the LGM (velocities lower than 45 m/yr masked out), whereas red dots indicate the location of the grid points used to estimate the individual ice streams deglaciation timing (Fig. 11). The time intervals for each location refer to its deglaciation timing range between the DATED-1 (Hughes et al., 2016) minimum and maximum reconstructions.

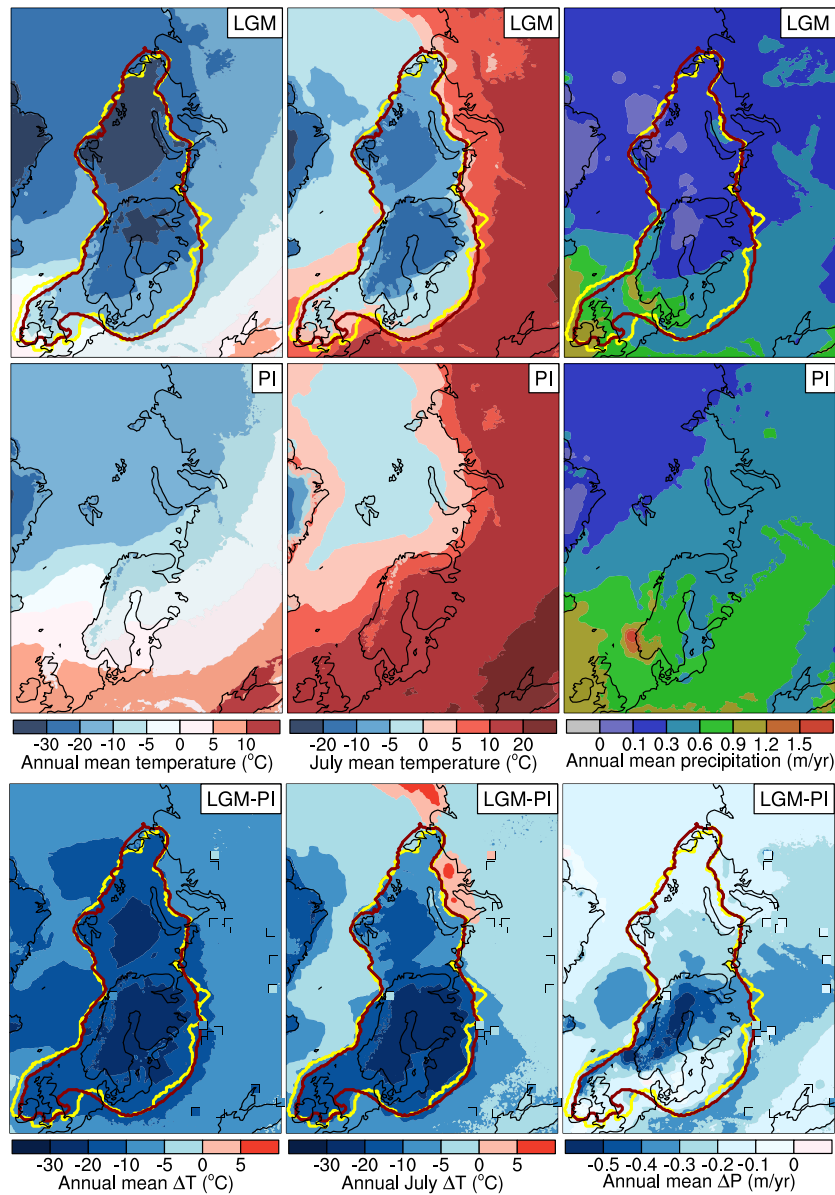


Figure 2: Reference climatology simulated with the IPSL-CM5A-LR AOGCM (Braconnot et al., 2012) interpolated into the ice sheet model grid. Top panels show annual mean temperature, July mean temperature and annual mean precipitation (left to right) at the LGM, whereas in the central panels the same fields are shown for PI. In the bottom panels, LGM - PI annual mean temperature, July mean temperature and annual mean precipitation anomalies are shown. The colored squares in the bottom panels show LGM - PI anomalies based on pollen data (Bartlein et al., 2011). In the top panels and bottom panels, red and yellow lines show the LGM ice sheet extent simulated in this study and from the ICE-5G reconstruction, respectively.

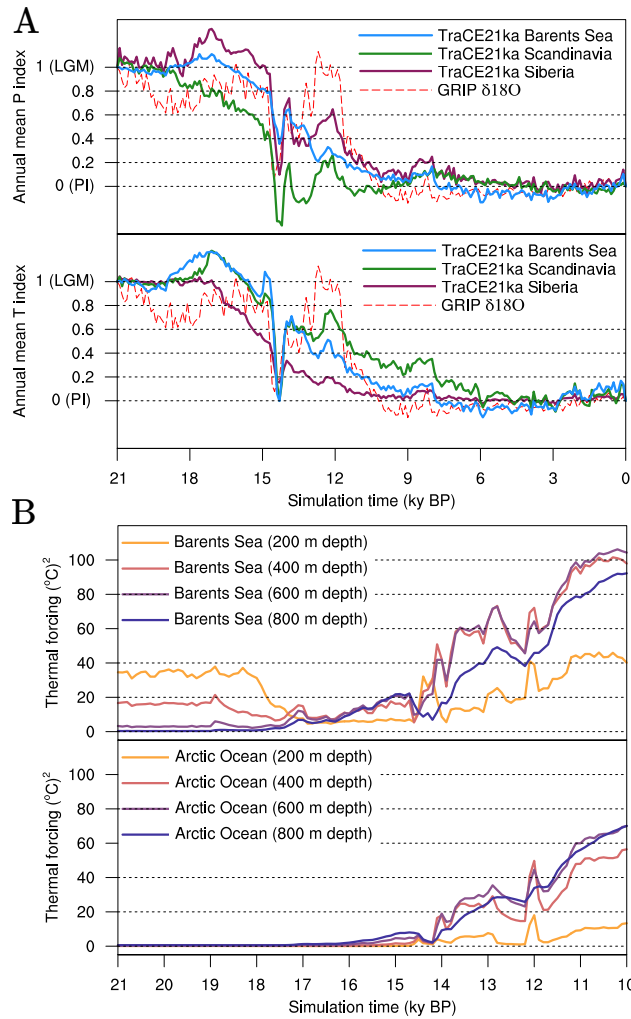


Figure 3: (A) TraCE21ka (Liu et al., 2009) macro-regional indexes (solid lines) for annual and July mean air temperature (top panel) and annual mean precipitation (bottom panel) used to progress between LGM and PI reference climatology during the transient simulations. For comparison, the index based on the NGRIP $\delta 18O$ record (Andersen et al., 2004) is shown in both panels (dashed red line). (B) Macro-regional ocean thermal forcing for the Barents Sea (top panel) and the Arctic Ocean (bottom panel) at typical grounding line depths (200, 400, 600 and 800 m) between 21 and 10 ky BP. The thermal forcing is computed based on the TraCE21ka (Liu et al., 2009) macro-regional ocean temperature and salinity profiles (see Figure S1) using Equations 7, 8.

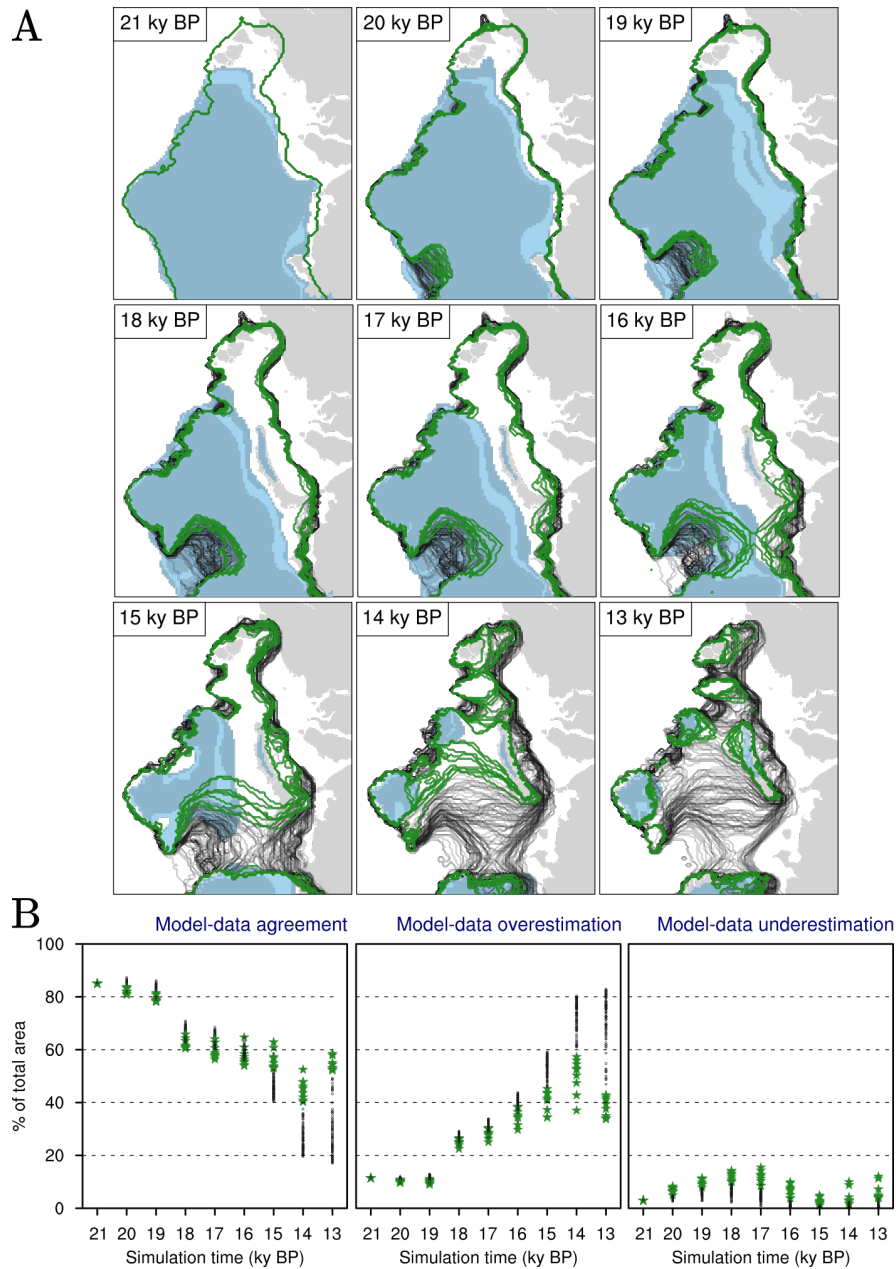


Figure 4: (A) Evolution of the simulated BSIS at 1000 yr time-slices between 21 and 13 ky BP for all the simulations in the ensemble (black lines). Admissible simulations (see Subsection 3.6) are shown in green. In the background, the DATED-1 min-mc-max scenarios are shown in light blue. (B) Simulated/DATED-1 ice sheet area agreement (left panel), overestimation (central panel) and underestimation (right panel) for all the members of the simulations ensemble between 21 and 13 ky BP. Admissible simulations (see Subsection 3.6) are marked in green.

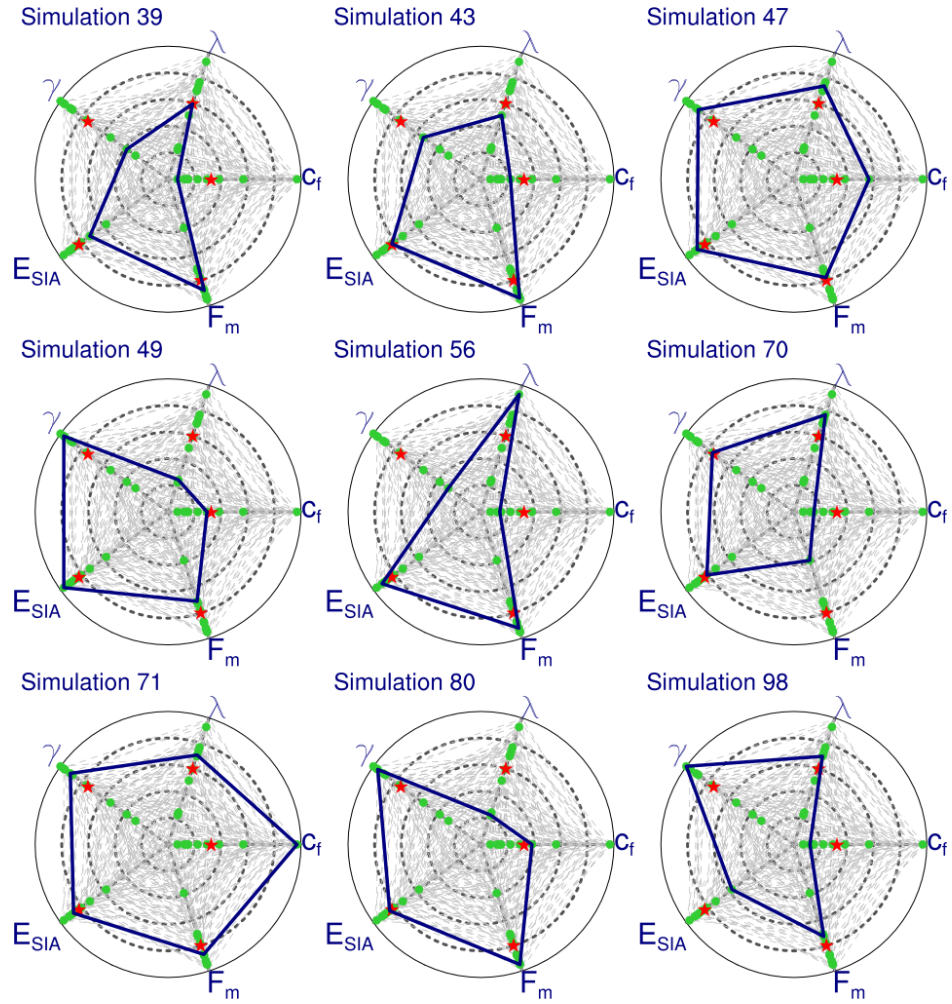


Figure 5: Radar plots showing the model parameters position within each range of values (normalized between 0, corresponding to the minimum values, and 1, corresponding to the maximum values, see Table 2) for all the admissible simulations (see Subsection 3.6). In each plot, the green polygon indicates the model parameters position relative to the individual simulation, whereas the green dots refer to the parameters position in the remaining admissible simulations. The red dots show the average parameter values in the admissible simulations, and the dashed grey polygons in the background show the combinations of model parameters for all the simulations in the ensemble.

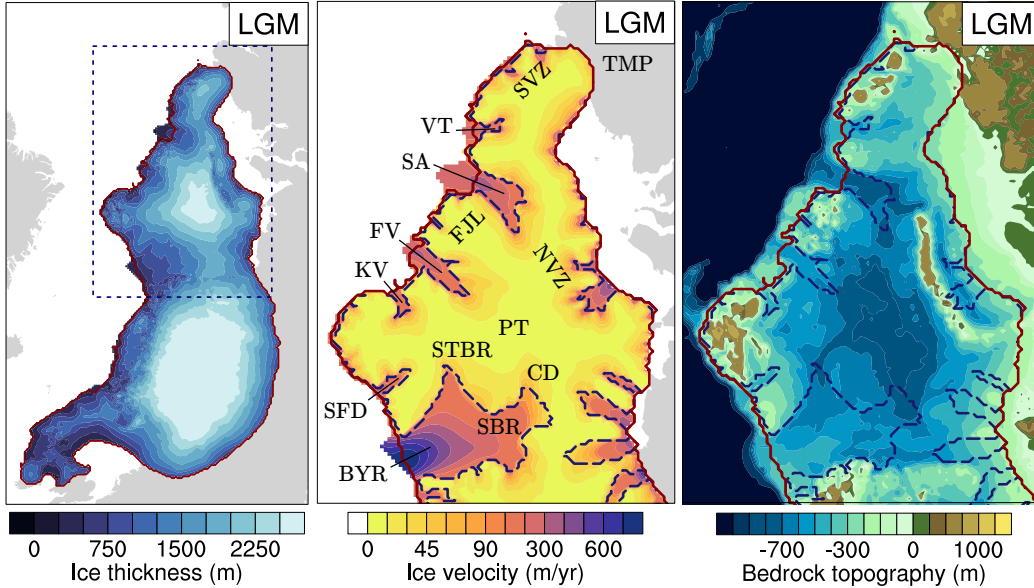


Figure 6: (A) Ice thickness of the simulated Eurasian ice sheets at the LGM. The blue dashed line indicates the region showed in panels (B) and (C). (B) Simulated ice velocities of the BSIS at the LGM. The blue dashed line indicates the boundary between regions treated with the SSA (ice streams and floating ice shelves) and with the SIA (inner part of the ice sheet) at the LGM. For clarity, we add abbreviations of the main geographic locations as follows: BYR = Bjørnøyrenna, SBR = Sentralbankrenna, CD = Central Deep, STBR = Storbankrenna, PT = Persey Trough, SFD = Storfjordrenna, KV = Kvitøya Trough, FV = Franz Victoria Trough, SA = St. Anna Trough, VT = Voronin Trough, FJL = Franz Josef Land, NVZ = Novaya Zemlya, SVZ = Severnaya Zemlya, TMP = Taimyr Peninsula. (C) Simulated isostatically depressed bedrock topography at the LGM in the BSIS region. Blue dashed line as in panel (B). In all the panels, the red line indicates the LGM simulated grounded ice limit.

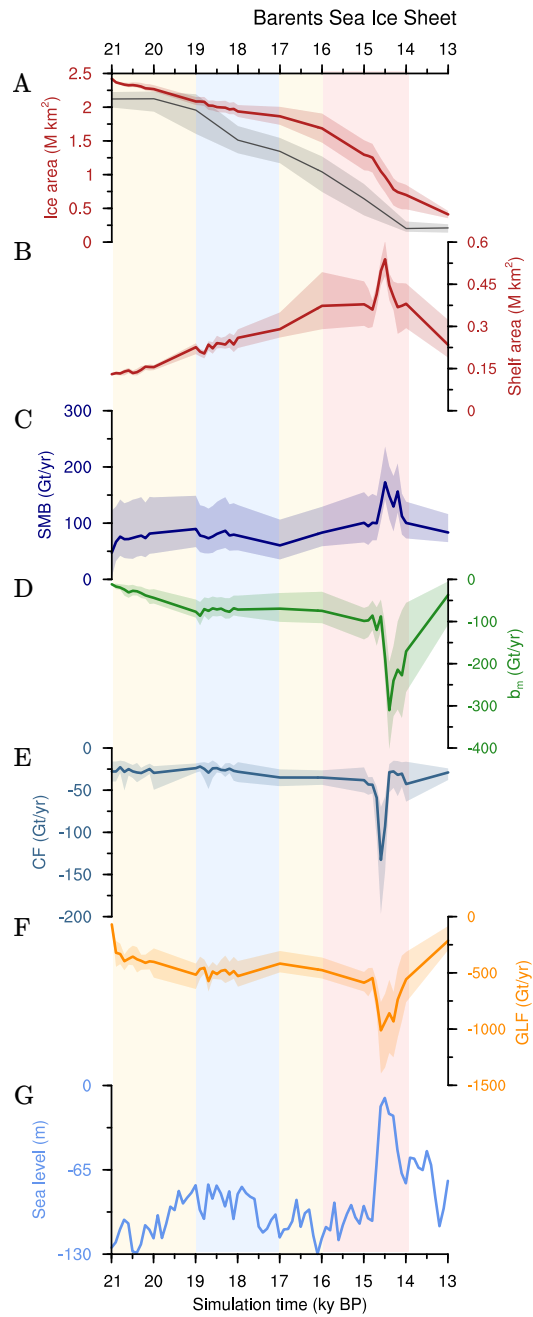


Figure 7: Time series of integrated (a) ice area, (b) ice shelf area, (c) SMB, (d) sub-shelf melting, (e) calving flux, (f) grounding-line flux for the BSIS in the minimum, maximum (shading) and average (solid lines) simulated scenario (see Subsection 3.6). The eustatic sea level prescribed in all the simulations of the ensemble is shown in (g).

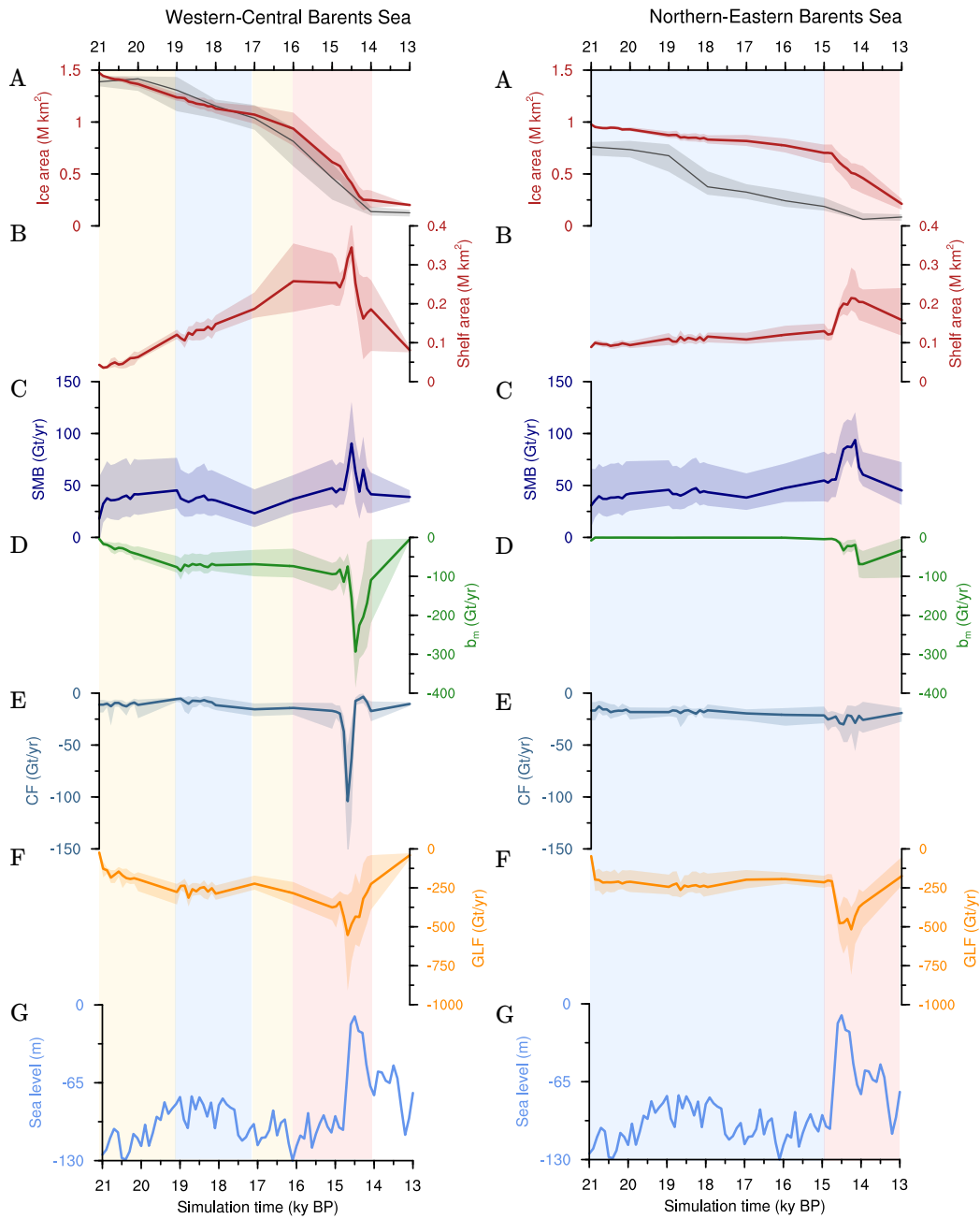


Figure 8: Left panel: time series of integrated (a) ice area, (b) ice shelf area, (c) SMB, (d) sub-shelf melting, (e) calving flux, (f) grounding-line flux for the western and central Barents Sea in the minimum, maximum (shading) and average (solid lines) simulated scenario (see Subsection 3.6). Right panel: same values as in the left panel are shown for the northern and eastern Barents Sea. In both panels, the eustatic sea level prescribed in all the simulations of the ensemble is shown in (f).

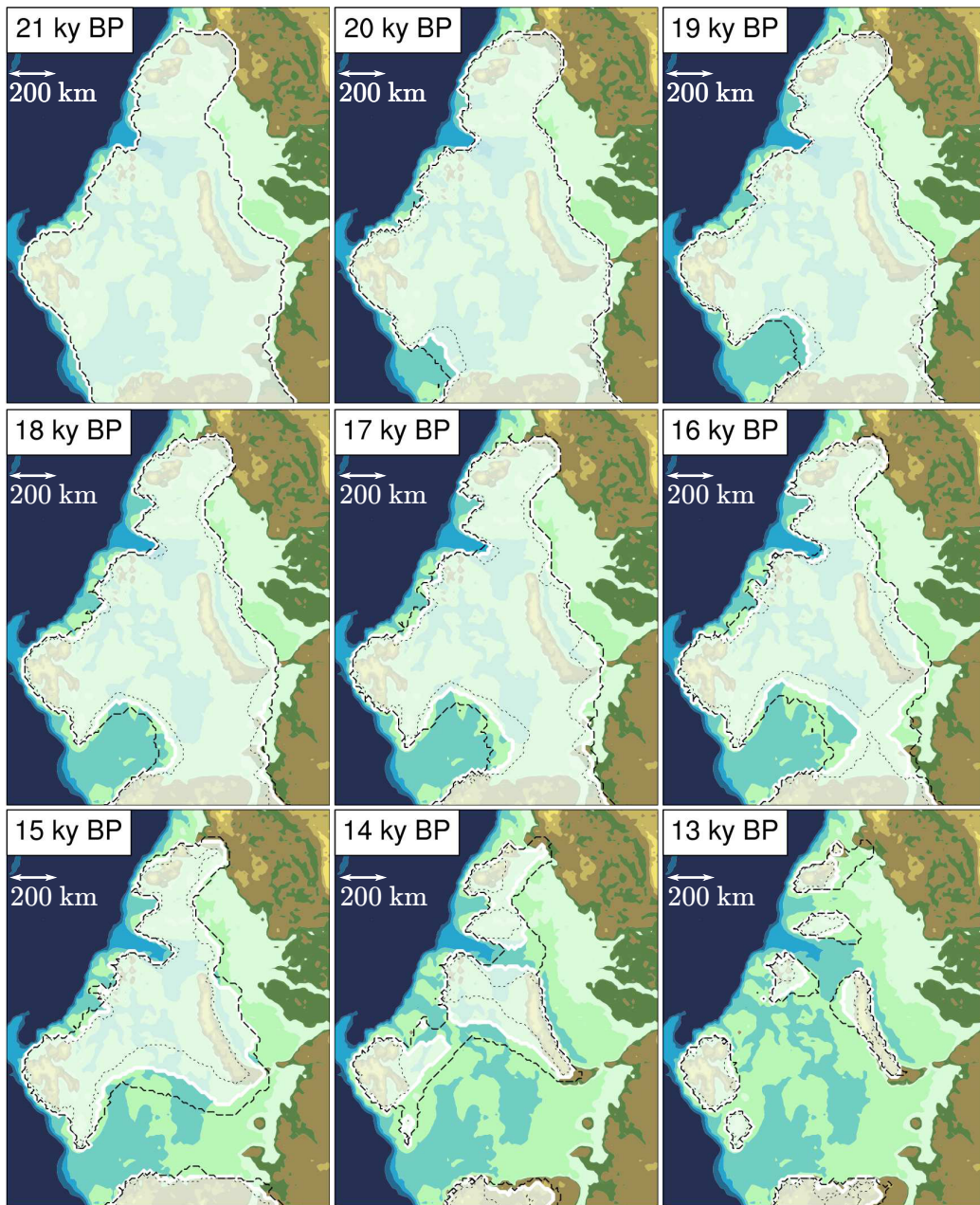


Figure 9: Evolution of the simulated BSIS at 1000 yr time-slices between 21 and 13 ky BP. White solid, black dashed and black dotted lines represent most-credible, maximum and minimum simulated scenarios, respectively. The simulated ice sheet extent in the most-credible scenario is also white filled. PI topography is showed in the background as a reference, with the same color legend as in Fig. 6c.

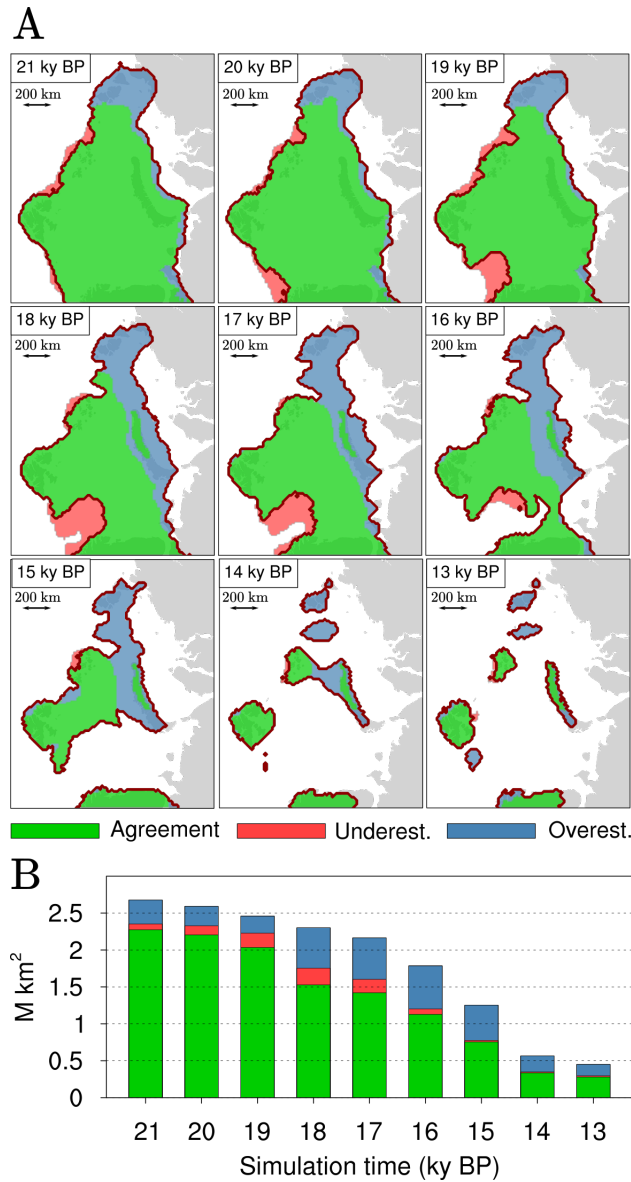


Figure 10: (A) Time-slice evolution of the model-data agreement between the min-max-avg simulated scenarios and the DATED-1 min-max-mc reconstruction between 21 and 13 ky BP, shown every 1000 years. The green area indicates region where there is model-data agreement, whereas red and blue areas indicate regions of model-data underestimation and overestimation, respectively (see Subsection 3.6). (B) Model-data agreement, underestimation and overestimation total area at each time slice shown in (A) and with the same color legend.

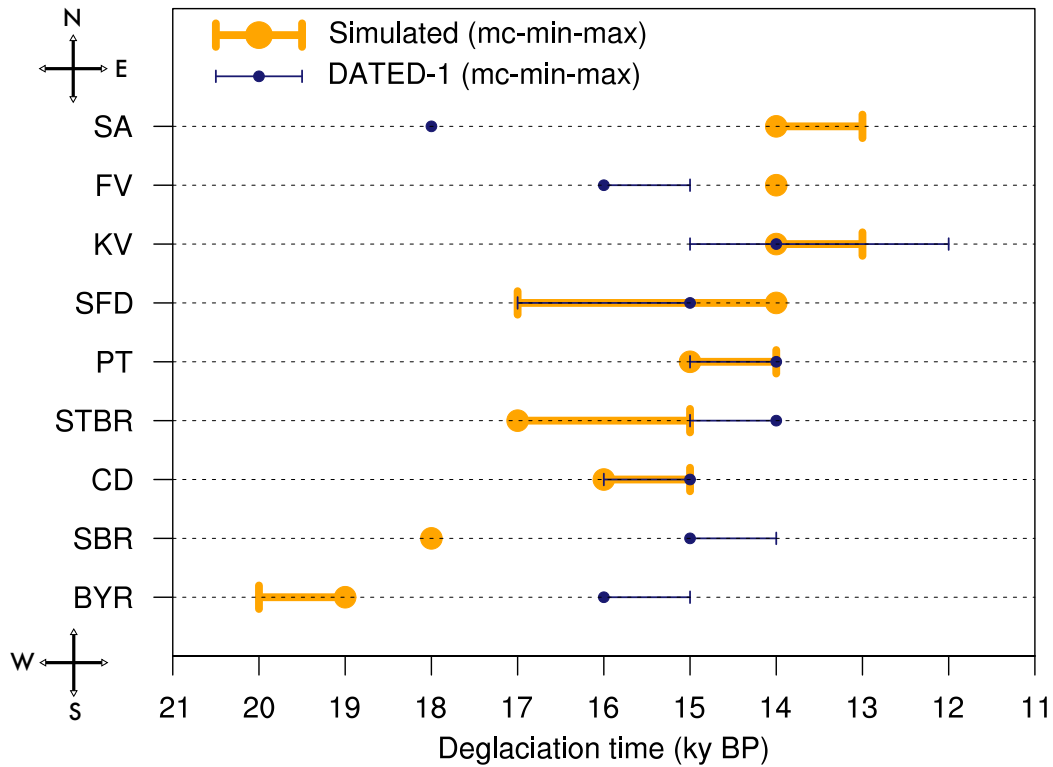


Figure 11: Simulated (orange dots and lines) and DATED-1 (dark blue dots and lines) deglaciation timing for the individual ice streams shown in Fig. 1. Dots represents the deglaciation timing in the average simulated scenario and DATED-1 most-credible reconstruction, whereas lines indicate the deglaciation timing in the minimum and maximum simulated and DATED-1 scenarios. As shown by the black arrow, the ice streams are ordered on the y-axis from south-west (SW) to north-east (NE). BYR = Bjørnøyrenna, SBR = Sentralbankrenna, CD = Central Deep, STBR = Storbankrenna, PT = Persey Trough, SFD = Storfjordrenna, KV = Kvitøya Trough, FV = Franz Victoria Trough, SA = St. Anna Trough.